UNIVERSIDADE FEDERAL DE SANTA CATARINA
CENTRO TECNOLÓGICO
PROGRAMA DE PÓS-GRADUAÇÃO EM ENGENHARIA QUÍMICA

Vinícius de Souza Godim de Oliveira

TiNb$_2$O$_7$ porous tapes prepared from TiO$_2$ and Nb$_2$O$_5$ aqueous suspensions by one-step rapid sintering/synthesis

Florianópolis
2020

Vinícius de Souza Godim de Oliveira

TiNb$_2$O$_7$ porous tapes prepared from TiO$_2$ and Nb$_2$O$_5$ aqueous suspensions by one-step rapid sintering/synthesis

Dissertação submetida ao Programa de Pós-Graduação em Engenharia Química da Universidade Federal de Santa Catarina para a obtenção do título de mestre em Engenharia Química.

Orientador: Prof. Dr. Sergio Yesid Gómez González
Coorientadores: Prof. Dr. Dachamir Hotza e Dr. Gilberto da Silva Falk

Florianópolis
2020

Vinícius de Souza Godim de Oliveira

$TiNb_2O_7$ porous tapes prepared from TiO_2 and Nb_2O_5 aqueous suspensions by one-step rapid sintering/synthesis

O presente trabalho em nível de mestrado foi avaliado e aprovado por banca examinadora composta pelos seguintes membros:

Prof. Agenor De Noni Jr, Dr.
Universidade Federal de Santa Catarina

Prof. Marco Di Luccio, Dr.
Universidade Federal de Santa Catarina

Certificamos que esta é a **versão original e final** do trabalho de conclusão que foi julgado adequado para obtenção do título de mestre em Engenharia Química.

_____

Coordenação do Programa de
Pós-Graduação

_____

Prof. Dr. Sergio Yesid Gómez González
Orientador

Florianópolis, 2020.

Este trabalho é dedicado aos jovens cientistas deste país.

AGRADECIMENTOS

RESUMO

$TiNb_2O_7$ (TNO, niobato de titânio) é um material cotado para uso em baterias de íon-lítio em substituição aos anodos de grafite atualmente empregados, além de ter sido estudado como fotocatalisador. A síntese desse óxido já foi explorada na literatura pelos métodos sol-gel, solvotérmico, hidrotérmico e micro-ondas, seguidos de calcinação para formar TNO, assim como síntese em estado sólido, compreendida como a reação entre TiO_2 e Nb_2O_5 que tem como produto TNO. Apesar disso, essa última foi apenas empregada para longos tempos de forno, na escala de horas. Neste trabalho, a síntese do niobato de titânio é realizada via reação em estado sólido através da técnica *fast firing*, sendo assim um exemplo de sinterização reativa rápida. Dessa maneira, a fase cristalina do óxido misto é formada em menos de 2 min. As amostras são *tapes* finos conformadas por *tape casting* aquoso. Apesar de não ser amplamente difundida na indústria, a aplicação da água como solvente é vantajosa em vários pontos de vista, incluindo o ambiental. Aditivos como dispersante, ligante, plastificante e anti-espumante são adicionados para obter um *tape* livre de trincas e flexível na sua forma *a verde*. Análises referentes ao processo como potencial zeta (ZP), análise termogravimétrica (TGA) e TGA diferencial (DTG), reologia, difração de raios X (XRD) e microscopia eletrônica de varredura (SEM) foram realizadas para caracterizar as amostras. Os resultados de ZP mostram que há pouca estabilidade para as partículas de TiO_2 utilizando o dispersante Darvan® C-N no pH da suspensão (pH = 6), porém a curva referente ao Nb_2O_5 apresenta boa estabilidade para essas partículas. Contudo, a suspensão foi estável o suficiente para ser processada em série desde a mistura dos ingredientes até a secagem do *tape*. A curva DTG apresentou picos no intervalo 200–500 °C, correspondendo à eliminação dos aditivos orgânicos. Assim, 500 °C e 600 °C foram escolhidas como as temperaturas de *debinding* para *tapes* sinterizados convencionalmente e via *fast firing* respectivamente. As curvas reológicas mostram um comportamento tixotrópico para suspensões muito carregadas em sólidos (ϕ = 45 vol.%), o que não é desejável por causar variação na viscosidade aparente e gerar *tapes* não-uniformes. Isso é mitigado reduzindo ϕ para 30 vol.%, que foi o valor escolhido para a otimização das amostras. Em termos de reologia, todas as curvas estudadas apresentaram caráter pseudoplástico, o que é preferível para *tape casting*. Resultados de XRD comprovaram a formação de $TiNb_2O_7$ pelo método *fast firing* nos primeiros 2 min de forno. Os precursores são o pó de TiO_2 (anatase pura, d_{50} = 0,26 μm) e uma mistura de Nb_2O_5 ortorrômbico e monoclínico (d_{50} = 0,967 μm). Imagens SEM mostraram um crescimento de grão significativo entre 2 e 5 min (78 %) de forno. Após 5 min, a cinética de crescimento é mais baixa (112 % de crescimento para 10 min em comparação a 2 min). Foi demonstrado que a variação no tempo de forno na ordem de minutos é uma maneira eficaz de ajustar a porosidade, medida pelo método de Arquimedes. A porosidade aberta foi similar à total para todas as amostras. *Tapes* sinterizados por *fast firing* foram significativamente porosos, com ε_{total} = 49 % para 2 min de tempo de forno; ε_{total} = 35 % para 5 min; e ε_{total} = 29 % para 10 min. *Tapes* sinterizados convencionalmente foram em comparação mais densos (ε_{total} = 13 %).

Palavras-chave: niobato de titânio. fast firing. tape casting. sinterização reativa.

RESUMO EXPANDIDO

Introdução

Ânodos para baterias de íon-lítio, que são a fonte de energia padrão em eletrônicos portáteis, compostos pelo material $TiNb_2O_7$ são cotados para substituir o grafite atualmente empregado. O niobato de titânio ($TiNb_2O_7$) possui características relevantes para tal função: uma capacidade teórica elevada de $387.6\,mAh\,g^{-1}$; um espaço bidimensional intersticial para a inserção de íons Li podendo conter até 5 átomos de Li por fórmula unitária ($Li_5TiNb_2O_7$); e uma tensão de operação acima de 1,0 V, o que previne a formação da interface sólido-eletrólito, que consome átomos de Li irreversivelmente, diminuindo a capacidade da bateria após o primeiro ciclo, e serve como base para o crescimento de dendritos que podem eventualmente perfurar o separador da bateria e causar um curto-circuito. Por ser um semicondutor, o $TiNb_2O_7$ também já foi estudado como material fotocatalítico. Métodos de síntese do niobato de titânio explorados da litertura incluem método solvotérmico, hidrotérmico, sol-gel para produção de um sólido precursor seguido de um tratamento à alta temperatura para formar a fase de $TiNb_2O_7$; e reação em estado sólido, compreendida como a reação TiO_2 + $Nb_2O_5 \longrightarrow TiNb_2O_7$. Essa última foi apenas estudada em longos tempos de forno, na escala de horas. Neste trabalho, a síntese do material é promovida concomitante à sinteração rápida (*fast firing*), sendo assim um exemplo de sinterização reativa, de forma que a fase cristalina do $TiNb_2O_7$ é formada em menos de 2 min de sinterização.

Objetivos

Os objetivos do trabalho envolvem a síntese do $TiNb_2O_7$ através de sinterização rápida e convencional a partir de TiO_2 e Nb_2O_5 conformados por *tape casting* com a reação em estado sólido entre esses óxidos ocorrendo durante a etapa de forno. Os objetivos específicos são: medir a composição, pureza e estabilidade coloidal da matéria-prima para determinar parâmetros de manufatura (de *tape casting*), através de difração de raios X e titulação do potencial zeta; estudar o comportamento reológico das suspensões variando a carga de sólidos para correlacionar com o processamento do *tape*; projetar os ciclos térmicos através de análise termogravimétrica; estudar a microstrutura, porosiade e densidade, composição, hidrofilicidade e constante dielétrica dos *tapes* sinterizados através de microscopia eletrônica de varredura, método de Arquimedes, difração de raios X, medida do ângulo de contato e medida dielétrica dependente da frequência, respectivamente para compreender a aplicação do material na forma de *tape*.

Metodologia

As suspensões foram preparados misturando água com dispersante (Darvan® CN). A essa mistura, TiO_2 (Anatase 1171 Kronos, d_{50} = 0,26 μm) e Nb_2O_5 (GO 350, grau óptico, d_{50} = 0,967 μm) foram separadamente adicionados na proporção molar 1:1. Bolas inertes de zircônia foram adicionadas e a suspensão foi colocada em um moinho de bolas, mantendo a agitação por 24 h. Após isso, ligante (Mowilith® LDM 6138), plastificante (polietileno glicol) e anti-espumante (Antifoam Y-30®) foram adicionados e a suspensão foi levada novamente ao moinho de bolas, mantendo-a sob agitação por 1 h. A suspensão permaneceu "em descanso" por 2 h para remover bolhas. Ela foi então conformada no *tape caster* (CC-1200, Mistler) usando uma espessura do *doctor blade* de 0,58 mm sobre o substrato Mylar® com uma velocidade da esteira de

$2\,mm\,s^{-1}$. O *tape* úmido foi seco por 24 h a temperatura e umidade ambiente. O *tape* foi cortado em quadrados de 3×3 cm e colocado no forno sob atmosfera de ar. Para o processamento via sinterização convecional, a primeira taxa de aquecimento foi de $1\,°C/min$ até atingir a temperatura de $500\,°C$, que foi mantida por 1 h. A segunda taxa de aquecimento foi de $5\,°C/min$ até atingir a temperatura de $1280\,°C$, que foi mantida por 2 h. Os *tapes* sinterizados por *fast firing* são processados de maneira similar: a primeira taxa de aquecimento foi de $1\,°C/min$ até atingir a temperatura de $600\,°C$, que foi mantida por 1 h, seguida por resfriamento até temperatura ambiente. Após isso, os *tapes* foram inseridos diretamente no forno pré-aquecido a $1300\,°C$ sob atmosfera de ar, sendo removidos após 2/5/10 min (3 amostras diferentes). As matérias-primas (TiO_2 e Nb_2O_5) foram analisadas por difração de raios X (XRD), titulação do potencial zeta (ZP) e titulação do tamanho médio de partícula. As suspensões foram caracterizadas pelo pH e pelo comportamento reológico. O *tape* a verde é caracterizado por análise termogravimétria (TGA e DTG). Os *tapes* sinterizados foram caracterizados por porosidade e densidade pelo método de Arquimedes, densidade real por picnometria com hélio, composição por difração de raios X, microestrutura por microscopia eletrônica de varredura (SEM), hidrofilicidade por ângulo de contato e constante dielétrica por medida dielétrica dependente da frequência.

Resultados e Discussão
Os difratogramas de raios X dos óxidos precursores TiO_2 e Nb_2O_5 comprovam a cristalinidade assim como a pureza desses materiais. O pó TiO_2 consiste de uma fase de anatase pura, enquanto o pó de Nb_2O_5 se trata de uma mistura de fases ortorrômbica e monoclínica. A titulação do potencial zeta demonstrou que há boa estabilidade para o Nb_2O_5 com o dispersante (Darvan® CN) com ZP = $-30\,mV$ para o pH da suspensão (pH = 6), enquanto para as partículas de TiO_2 com dispersante, há pouca estabilidade devido à proximidade do ponto isoelétrico, em que ZP = 0. De forma geral, isso não foi um problema para o processamento, provavelmente devido à falta de um tempo de armazenamento mais longo, visto que a suspensão descansa apenas 2 h após o período de agitação no moinho de bolas, antes de ser conformada por *tape casting* e então seca. O tamanho médio de partícula para o Nb_2O_5 apresentou um pico próximo ao ponto isoelétrico em pH = 4,21, o que é esperado devido à aglomeração de partículas quando não há um mecanismo eletrostático de repulsão entre as mesmas. Os resultados de reologia revelaram que há comportamento pseudoplástico para suspensões com carga de sólidos na faixa testada 30–45 vol.%, o que é ideal para *tape casting*. Para suspensões muito concentradas (45 vol.%), observou-se caráter tixotrópico, que não é desejável para *tape casting*. Assim, escolheu-se a carga de sólidos de $\phi = 30$ vol.% para otimização da formulação. Ao ajustar os dados reológicos a uma lei de potência $\tau = k\dot{\gamma}^n$ (modelo de Ostwald), notou-se uma influência mais forte da carga de sólidos no índice de consistência (k) e menos acentuada sobre o índice de comportamento (n). Análise termogravimétrica (TGA) e a correspondente análise diferencial (DTG) demonstraram as temperaturas em que ocorre a queima dos aditivos orgânicos, mais acentuada na faixa $200–500\,°C$. Trincas formadas no *tape* a verde após a secagem foram um problema comprometedor no processamento e puderam ser contornadas adicionando um plastificante (polietileno glicol) para a otimização da formulação dos *tapes*. Foi demonstrado que o ajuste no tempo de forno para o *fast firing* é uma maneira de controlar a porosidade do *tape* sinterizado. A porosidade total foi de 49%, 35% e 29% para os tempos de 2, 5 e 10 min respectivamente. *Tapes* sinterizados convencionalmente foram significativamente menos porosos: ($\varepsilon_{total} = 13\%$). Os

valores de porosidade aberta foram similares aos de porosidade total, indicando que o espaço poroso é interconectado. Os difratogramas de raios X para todos os *tapes*, tanto preparados via *fast firing* quanto por sinterização convencional, apresentaram os mesmos padrões e foram compatíveis com o padrão da literatura para o $TiNb_2O_7$. As imagens de microscopia eletrônica de varredura mostram um crescimento de grão significativo no intervalo entre 2 e 5 min e menor entre 5 e 10 min de *fast firing*. Utilizando o mesmo método, as imagens do *tape* sinterizado convencionalmente apresentaram grãos em formato diferenciado: prismas regulares alongados. Propõe-se a hipótese de que essa forma está associada ao hábito do cristal de fase monoclínica. A constante dielétrica dos *tapes* preparados via *fast firing* apresentou variação similar com a frequência quando comparados com *tapes* preparados via sinterização convencional. O valor da constante dielétrica para frequência zero foi ~ 10, similar à constante dielétrica do grafite.

Considerações Finais
O trabalho foi bem sucedido quanto a síntese do $TiNb_2O_7$ através da reação em estado sólido $TiO_2 + Nb_2O_5 \longrightarrow TiNb_2O_7$ ocorrendo durante sinterização rápida, com a fase cristalina monoclínica sendo formada em menos de 2 min. A tecnologia de *tape casting* foi empregada para a conformação das amostras, sendo que a formulação dos *tapes* foi otimizada variando a carga de sólidos e o conteúdo de plastificante, para promover *tapes* de espessura uniforme e sem trincas.
Palavras-chave: niobato de titânio. fast firing. tape casting. sinterização reativa.

ABSTRACT

TiNb$_2$O$_7$ (TNO, titanium niobate) is a sought material for use in lithium ion batteries to replace graphite anodes currently employed, besides having been studied as a photocatalyst. The synthesis of this oxide has already been explored in the literature by sol-gel, solvothermal, hydrothermal and microwave methods, followed by calcination to form TNO, as well as solid state reaction, comprehended as the reaction between TiO$_2$ and Nb$_2$O$_5$ to yield TNO. Nevertheless, the latter has only received attention for long furnace times, on the scale of hours. In this work, the synthesis of titanium niobate is performed via solid state reaction using *fast firing*, thus being an example of rapid reactive sintering. In this case, the crystalline phase of the mixed oxide is formed in less than 2 min. The samples are thin tapes shaped by aqueous tape casting. Although not widely used in industry, the application of water as a solvent is advantageous from various points of view, including the environmental perspective. Additives such as dispersant, binder, plasticizer and defoamer are added to obtain a flexible and crack-free tape in its green form (pre-sintering). Analysis and measurements such as zeta potential (ZP), thermogravimetric analysis (TGA) and differential TGA (DTG), rheology, X-ray diffraction (XRD) and scanning electron microscopy (SEM) were performed to characterize the samples in the various steps of processing. ZP results showed that there was poor stability for TiO$_2$ particles using Darvan® CN as a dispersant at the pH of the suspension (pH = 6), but the titration curve for Nb$_2$O$_5$ exhibited good stability for these particles. In general, the suspension was stable enough to be processed from ingredient mixing to drying. The DTG curve showed main peaks in the interval 200–500 °C corresponding to the elimination of organic additives. 500 °C and 600 °C were then chosen as the debinding temperatures for conventionally sintered and fast-fired tapes respectively. The rheological curves exhibited a thixotropic behavior for heavily loaded suspensions (solids loading ϕ = 45 vol.%). This undesirable effect in tape casting (due to changes in the apparent viscosity with time, thus generating non-uniform tapes) is mitigated by reducing ϕ to 30 vol.%. In terms of rheology, all samples displayed pseudoplastic character, which is preferable for tape casting. XRD results proved the formation of TiNb$_2$O$_7$ by *fast firing* in the first 2 min of furnace time. The precursors are pure anatase TiO$_2$ powder (d_{50} = 0.26 µm) and a mixture of orthorhombic and monoclinic Nb$_2$O$_5$ (d_{50} = 0.967 µm). SEM images showed significant grain growth in the 2 to 5 min interval (growth of 78 %). The grain growth kinetics is slower after 5 min (growth of 112 % for 10 min with respect to 2 min). It was possible to adjust porosity, measured by the Archimedes method, by changing the holding time within the range of 2–10 min. The open porosity was very close to the total porosity for all samples. The fast-fired tapes were significantly porous, with ε_{total} = 49 % for a holding time of 2 min; ε_{total} = 35 % for 5 min; and ε_{total} = 29 % for 10 min. Conventionally sintered tapes were conversely much denser (ε_{total} = 13 %).

Keywords: titanium niobate. fast firing. tape casting. reactive sintering.

LIST OF FIGURES

LIST OF TABLES

LIST OF ABBREVIATIONS AND ACRONYMS

CS   conventional sintering / conventionally sintered tape

DLS   dynamic light scaterring

DTG   differential thermogravimetric analysis

FF   fast firing

FF2   fast-fired tape at a holding time of 2 min

FF5   fast-fired tape at a holding time of 5 min

FF10   fast-fired tape at a holding time of 10 min

SI   International System of Units

SOFC   solid oxide fuel cell

TGA   thermogravimetric analysis

TNO $TiNb_2O_7$

XRD   X-ray diffraction

ZP   zeta potential

LIST OF SYMBOLS

A surface area

d_{50} median value of the particle size distribution

E_g band gap

g acceleration of gravity

k flow consistency index

M molar mass

m sample mass

n flow behaviour index

R Pearson correlation coefficient

R_h particle hydraulic radius

S solids (subscript)

v terminal velocity

W water (subscript)

ε porosity

η suspension dynamic viscosity

$[\eta]$ intrinsic viscosity

γ surface energy

$\dot{\gamma}$ shear rate

μ solvent dynamic viscosity

ω mass fraction

ϕ solid volume fraction

ϕ_m maximal solid volume fraction

ρ density

τ shear stress

τ_0 yield stress

CONTENTS

1 INTRODUCTION

TiNb$_2$O$_7$ (TNO, titanium niobate) is a promising candidate as an anode material for lithium-ion batteries (LIBs) to substitute graphitic carbon (HAN; HUANG; GOODE-NOUGH, 2011). LIBs are the standard batteries in modern portable electronics and are now also being utilized in electric vehicles (KANG et al., 2006). The remarkable features of LIBs, which provide safe, compact and lightweight energy storage, which are particularly pertinent when combined with clean energy sources, led to the 2019 Nobel Prize in chemistry, awarded to John Goodenough[1], M. Stanley Whittingham and Akira Yoshino for the development of this technology.

TNO has also been applied as a photocatalyst (FALK; BORLAF, et al., 2018) due to its semiconducting character. There are many known routes to synthesize this oxide, yet the solid-state reaction between TiO$_2$ and Nb$_2$O$_5$ is regarded as the simplest and most cost-effective one, especially for the large-scale production (CHOI et al., 2017).

In this work, titania (TiO$_2$) and niobia (Nb$_2$O$_5$) are mixed in an aqueous dispersion with proper organic additives, cast as a tape (via tape casting), dried and calcined in air. In the furnace, after debinding, the solid state reaction between the oxides occurs alongside the typical mechanisms of sintering: densification and grain growth. This combination of thermally-activated phenomena is called reactive sintering (or reaction sintering). When the precursors (titania and niobia) are added in a 1:1 molar ratio, the complete conversion into TiNb$_2$O$_7$ is thermodynamically favoured and is kinetically activated at high temperatures. Hence we have the formation of a new phase (monoclinic TiNb$_2$O$_7$) with the output product being a thin flat sheet (tape) of this material.

The sintering step was carried in two different ways: either conventional sintering (CS) or fast firing (FF), also known as rapid sintering. In CS, the sample, after debinding at a lower temperature (e.g. 500 °C), is slowly heated to the target temperature (e.g. 1300 °C) and is kept at that temperature for a significant *holding* time (e.g. 2 h), followed by cooling to room temperature. In FF, the green body is, after debinding, placed directly inside a furnace which is already heated at the higher target temperature and is removed after a few minutes (2–10 min in this work). Thus, given a chemical reaction is occuring concomitant to fast firing, we explore a particular case of rapid reactive sintering.

The thin tape geometry is advantageous when it comes to minimizing temperature gradients in the body during the thermal treatment in order to promote homogeneous densification, given heat transfer is a limiting factor for controlling the microstructural evolution when fast firing is applied as a sintering method (POSSAMAI et al., 2012).

The benefit of fast firing is energy and time savings due to low furnace times

---

[1] In the realm of the science of LIBs, John Goodenough also did research on TiNb$_2$O$_7$· as an anode material (HAN; GOODENOUGH, 2011; HAN; HUANG; GOODENOUGH, 2011)

as well as the mitigation of grain growth. This can be an advantage since fine-grained materials have special electrical, mechanical, optical and thermal properties (GÓMEZ et al., 2016). In the case of anode materials for LIBs, the electrode-electrolyte contact area and the grain size, which is directly related to the diffusion length of Li ions, are key parameters concerning the electrochemical performance (HU, Y.-S. et al., 2006). Regarding its photocatalytic application, a high surface area is naturally needed for heterogeneous catalysis, since the active sites at the surface provide the reactivity. Therefore, fine-grained materials with the proper structural properties and a high surface area are appealing for these two applications, and fast firing may be an appropriate method for their manufacturing.

1.1 OBJECTIVES

1.1.1 General objective

The objectives of this work are focused on synthesizing $TiNb_2O_7$ from tape-cast TiO_2 and Nb_2O_5 mixture via fast firing and conventional sintering with a solid state reaction taking place between the precursor oxides.

1.1.2 Specific objectives

a) To assess the starting materials (TiO_2 and Nb_2O_5) composition and colloidal stability to determine manufacturing parameters of tape casting, through X-ray diffraction (XRD) analysis and zeta potential (ZP) titrations.

b) To study the suspension rheological behaviour varying the solids loading to correlate the outcome of rheological measurements with the tape processing.

c) To design the thermal cycles intended for tape manufacturing with the knowledge gained from thermogravimetric analysis (TGA).

d) To optimize the slurry formulation in terms of the additive contents, specially the binder and plasticizer contents, in order to obtain a crack-free and malleable tape in its green form and a cohesive sintered body.

e) To study the microstructure, porosity and bulk density, composition, hydrophilicity and relative permittivity of the as-prepared sintered tapes through scanning electron microscopy (SEM), Archimedes method, X-ray diffraction (XRD), contact angle measurement and frequency-dependent dielectric measurement respectively to disclose the applicability of the sintered bodies (tapes).

2 LITERATURE REVIEW

2.1 SYNTHESIS AND APPLICATION OF TITANIUM NIOBATE

$TiNb_2O_7$ (TNO, titanium niobate) was first mentioned in the work of Roth and Coughanour (1955), which investigated the phase equilibria of TiO_2-Nb_2O_5 systems. Exploring its semiconducting properties, it was proposed as a photoanode for a photo-electrochemical cell by De Haart, Boessenkool, and Blasse (1985). Later Reich, Kaiser, and Irvine (2001) studied its performance as an solid oxide fuel cell (SOFC) anode.

Yet it was not until the work of Han, Huang, and Goodenough (2011) that it was tested as an anode material in a lithium-ion battery (LIB), which laid the foundation for most of the research that followed on the synthesis and application of TNO. The main aspects of TNO that favour its electrochemical applicability are: a high theoretical specific capacity of 387.6 $mAhg^{-1}$ given by the overlapping redox pairs Ti(IV)/Ti(III), Nb(V)/Nb(IV) and Nb(IV)/Nb(III); a 2D interstitial space for the insertion of Li ions, which contains up to 5 Li atoms per formula unit ($Li_xTiNb_2O_7$, $0 \le x \le 5$); and a high operating voltage of 1.6 V vs Li^+/Li (compared to 0.2 V for graphite), which prevents the formation of the solid-electrolyte interphase (SEI): a passivating layer which robs Li irreversibly in the first cycle and serves as a basis for the growth of Li dendrites on fast charging, which may attack the separator of the battery - a porous membrane that allows the passage of Li ions but is impermeable to the flow of electrons -, causing a short circuit (HAN; HUANG; GOODENOUGH, 2011). The SEI layer forms whenever the operating voltage vs Li^+/Li is < 1.0 V.

In order to study it as a SOFC anode, Reich, Kaiser, and Irvine (2001) synthe-sized TNO by a solid state reaction by mixing TiO_2 and Nb_2O_5 in acetone, followed by drying and sintering at 1250 °C for 48 h in air. The conversion of these oxides into $TiNb_2O_7$ using a solid state method is thermodynamically favoured when they are mixed in a 1:1 molar ratio, as indicated by the TiO_2-Nb_2O_5 phase diagram (Figure 1) and is kinetically activated at high temperatures.

Han, Huang, and Goodenough (2011) prepared TNO to be used an as anode material by a sol-gel procedure. They mixed Nb_2O_5 with HF to create a transparent so-lution and then with NH_3 to obtain a $Nb(OH)_5$ precipitate. The precipitate was dissolved in citric acid and a water-ethanol solution containing $Ti(OC_3H_7)_4$ was added while the pH was adjusted with NH_3. This mixture contained Nb^{5+} and Ti^{4+} ions and formed a citric gel at 90 °C. By heating to 140 °C, a precursor was obtained, which was then annealed at 900–1350 °C to form TNO. In the same work, they synthesized a different structure named DTNO by the solid state reaction between TiO_2 and Nb_2O_5 for 24 h at 900-1110 °C. DTNO, which means $Ti_{1-y}Nb_yNb_2O_7$ (with y = 0.1), was said to be more electronically conductive than TNO.

Despite its promising electrochemical properties, pristine $TiNb_2O_7$ presents

Figure 1 – Phase diagram of the TiO_2-Nb_2O_5 system
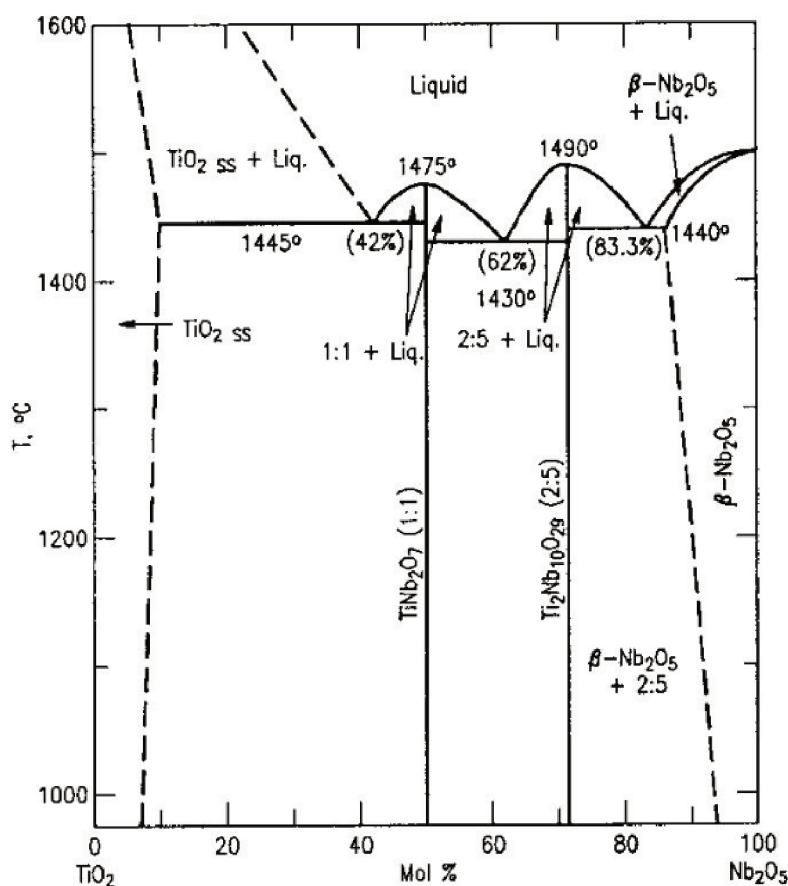
Source: Babich et al. (1988)

nonetheless some flaws for that use: a low intrinsic electronic conductivity and low ionic diffusivity, mainly derived from its large band gap ($E_g > 2\,eV$) (PARK; SONG; PAIK, 2015). Therefore, many of the works in the field concentrate on doping, coating and other forms of introducing a secondary more conductive species. Also in the work of Han, Huang, and Goodenough (2011), for instance, they prepared carbon-coated TNO and DTNO, which enhanced electronic conductivity, by ball milling the TNO and DTNO samples into a fine powder and adding a sucrose solution. After drying, the precursors were annealed at 550 °C for 6 h in argon atmosphere. The synthesized TNO had a grain size of ~ 10 µm.

In the same year, Lu et al. (2011) investigated the lithium storage mechanism in TNO and synthesized it via a solid state reaction, by mixing TiO_2 and Nb_2O_5 powders in ethanol and ball milling for 1 h. The samples were then dried and heated to 1350 °C for 24 h at a heating rate of 5 °C/ min. The obtained grain size was 20 µm.

Considering the works mentioned above resulted in grain sizes in the micrometric range, the first report on nanostuctured $TiNb_2O_7$ was then made by Tang et al. (2013). Their process was as follows: they prepared a solution of polyvinylpyrrolidone, niobium

ethoxide ($Nb(OC_2H_5)_5$) and tetrabutyl orthotitanate ($Ti(OC_4H_9)_4$), which is electrospun into nanofibers and then calcined at 1000 °C for 5 h with a heating rate of 2 °C/min. The resulting fibers were named nano-pearl-strings for the attached single-crystallites microstructure. Tested as anodes for LIBs, the material exhibited superior performance in terms of rate capability and capacity retention upon cycling compared to previous works. They attributed these results to favourable kinetics of a 1D nanostructure. As a matter of fact, shorter grain sizes and a high surface area translate to shorter transport lengths for Li^+ and higher electrode-electrolyte contact area (HU, Y.-S. et al., 2006), which are desirable for anodes in LIBs. As a consequence, a large part of the research that followed focused on reducing grain size down to the nanometric range to improve electrochemical kinetics.

Fei et al. (2013) synthesized nano-sized TNO by dissolving $NbCl_5$ in ethanol and then adding $Ti(OC_3H_7)_4$ with subsequent drying and annealing at 1000 °C for 5 h in air (with a heating rate of 2 °C/min). By adding nanostructured mesoporous silica (SBA-15) at the mixing phase with final etching by NaOH solution, they could achieve a smaller grain size of 10 nm, compared to > 100 nm for samples without SBA-15.

Aravindan et al. (2014) synthesized TNO nanofibers to be used as an insertion anode for lithium ion capacitors via an electrospinnning technique. In their synthesis, they dissolved polyvinylpyrrolidone (PVP) in ethanol, to which titanium(IV) butoxide and niobium(V) ethoxide were added and stirred for 1 h. With the addition of acetic acid, the polymer solution was then elestrospun. Finally, the fibers were preheated at 300 °C for 1 h and then calcined at 1000 °C for 4 h with a heating rate of 5 °C/min.

Guo et al. (2014) studied highly porous TNO with nano-sized pore channels for the access of Li^+ by diffusion into the particle bulk. The material was synthesized via sol-gel method, using $Nb(OC_2H_5)_5$ and $Ti(OC_4H_9)_4$ as precursors and commercial block-polymer F127 as surfactant. The surfactant molecules formed micelles that were pyrolyzed to form a mesoporous structure.

Jat et al. (2014) studied the heat capacity of TNO and synthesized it via a solid state reaction method by mixing stoichiometric amounts of TiO_2 and Nb_2O_5 with ethanol as the mixing reagent, followed by heating pelletized samples to 1000 °C for 48 h.

Jayaraman et al. (2014) synthesized electrospun TNO fibers. They mixed polyvinylpyrolidone (PVP) with titanium (IV) butoxide and niobium (V) ethoxide using ethanol as solvent. After obtaining a homogeneous polymer solution, they added acetic acid and stirred for 12 h. The sol-gel solution was then electrospun. The prepared fibers were heated for 1 h at 300 °C and then sintered at 1000 °C for 4 h with a heating rate of 5 °C/min under air atmosphere.

In the work of Jo et al. (2014), a highly ordered mesoporous TNO structure was achieved by mixing titanium isopropoxide, niobium ethoxide, structure-directing agent

(ethylene oxide)-*b*-poly(styrene) (PEO-*b*-PS) and small amount of tetraethyl orthosilicate (TEOS). The process is known as evaporation-induced self-assembly (EISA). After heat treatment and silica etching, the mesoporous structure had a crystal size of 15 nm and a pore size of 40 nm and high surface area ($74\,m^2g^{-1}$). Concerning the performance as an anode, the material presented a capacity of $289\,mAhg^{-1}$ at 0.1 C rate (1 C corresponding to the theoretical value of $387\,mAg^{-1}$), $162\,mAhg^{-1}$ at 20 C and $116\,mAhg^{-1}$ at 50 C.

Ashish et al. (2015) studied the performance of hybrid $TiNb_2O_7$/graphene as an anode material synthesized via a solvothermal method. They dispersed titanium isopropoxide, niobium ethoxide and graphene oxide in acetic acid, followed by a solvothermal reaction at 200 °C for 24 h. The synthesized precipitate was annealed at 900 °C for 5 h in argon atmosphere, which reduced the graphene oxide, as well as crystallized the TNO particles. The resulting particle size was ∼ 25–30 nm.

Cheng et al. (2015) synthesized porous $TiNb_2O_7$ nanospheres comprised of nanoparticles with the assistance of blockpolymer P123 by a hydrothermal method. The blockpolymer was dissolved in ethanol, then $NbCl_5$ and $Ti(OC_4H_9)_4$ were added. The hydrothermal reaction was then carried in an autoclave at 220 °C for 16 h. The as-produced white precipitate was washed and dried, then annealed at 800 °C for 5 h with a heating rate of 5 °C/min. The obtained TNO crystals had a size of 43 nm and the nanospheres had a diameter of 500 nm.

Lou, Ma, et al. (2015) synthesized TNO nanorods by a sol-gel method. They mixed Nb_2O_5 with a HF solution, stirring for 4 h at 70 °C. $(NH_4)OH$ was added which precipitated $Nb(OH)_5$. After filtering, washing and drying, the solid was added to an oxalic acid solution, which produced a solution of Nb^{5+} ions. In parallel, $Ti(OC_4H_9)_4$ was mixed with ethanol and oxalic acid and this solution was mixed with the Nb^{5+}-containing solution. The mixture was heated to 90 °C to remove the solvents. The obtained powder was calcined at 900 °C in air. The resulting material consisted of TNO nanorods with 300–600 nm in length and 100–300 nm in diameter.

Park, Song, and Paik (2015) prepared TNO nanofibers decorated with conductive material $Ti_{1-x}Nb_xN$. They prepared a first solution made of $Ti(OC_4H_9)_4$ with $Nb(OC_2H_5)_5$ in ethanol, *N-N*-DMF and acetic acid. A second solution was prepared with ethanol, *N-N*-DMF and polyvinylpyrrolidone (PVP). Both solutions were mixed and then electronspun. The obtained fibers were calcined at different temperatures (550/700/850/1000 °C) in air for 5 h with a heating rate of 5 °C/min. The decoration of the fibers was done by thermal ammonia gas treatment. By running an Ar-NH_3 gas mixture over the samples at 600-700 °C for 10/30/60 min, $Ti_{1-x}Nb_xN$ was formed on the surface of the nanofibers, which improved electronic conductivity. The nanofibers had diameters of 70/110/210 nm, depending on the concentration of the solutions.

The work of Park, Wu, et al. (2015) also relied on nitridation (formation of

$Ti_{1-x}Nb_xN$ at the surface) as a method to improve electronic and ionic conductivity. In their work, $TiNb_2O_7$ porous microspheres were synthesized via a solvothermal reaction. Diethylenetriamine (DETA) was dissolved in isopropyl alcohol followed by the additions of $Ti(OC_4H_9)_4$ and $Nb(OC_2H_5)_5$ with stirring. The solution was transferred to an autoclave, which was put inside an oven at 200 °C for 12 h. The powder is removed by washing and drying then calcined at 700 °C in air for 5 h with a heating rate of 5 °C/min. Nitridation was also performed by thermal ammonia gas treatment, as in the work of Park, Song, and Paik (2015).

Wang and Shen (2015) studied the performance of $TiNb_2O_7$ at carbon as a lithium-ion hybrid electrochemical supercapacitor, which incorporates a lithium-ion battery-type anode as a capacitor-type cathode. In their synthesis, a sol-gel method was employed. Polyacrylonitrile (PAN) was dissolved in *N-N*-dimethylformamide (DMF) with subsequent addition of a $NbCl_5$ and $Ti(OC_4H_9)_4$ solution in DMF and stirred for 12 h. The prepared solution was then electrospun. After spinning, the fibers were dried at 80 °C for 24 h and then calcined at 1000 °C for 5 h in air with a heating rate of 2 °C/min. In order to incorporate carbon, the obtained fibers were mixed with a glucose solution, dried and then calcined at 600 °C for 2 h in N_2 atmosphere.

Wen et al. (2015) synthesized TNO doped with vanadium ($TiNb_{1.98}V_{0.02}O_7$) via solid state method. They mixed TiO_2, Nb_2O_5, V_2O_5 and polyvinylpyrrolidone with ethanol as a solvent. The mixture was dried and then pre-heated at 800 °C for 6 h and sintered at 1200 °C for 12 h. V-doping was said to be effective in enhancing the lithium ion diffusion.

Daramalla et al. (2016) used a solid state reaction to synthesize TNO and then ablated it onto a Pt(200)/TiO_2/SiO_2/Si(100) substrate by pulsed laser deposition. They used TiO_2 and Nb_2O_5 as starting materials and performed calcination at 1350 °C for 24 h in air. After milling the powder again, they sintered it further at 1350 °C for 24 h.

Lei Hu et al. (2016) synthesized TNO nanorods via a sol-gel method with a sodium dodecyl surfate (SDS) surfactant. In their synthesis, SDS is mixed with acetic acid, HCl solution, $NbCl_5$ and ethanol, with subsequent addition of $Ti(OC_3H_7)_4$. The mixture was then dried at 80 °C for 12 h and calcined at 700 °C for 2 h in air.

Noh and Choi (2016) prepared TNO microspheres made of primary nanoparticles using a hydrothermal reaction. They mixed titanium isopropoxide with ethanol and acetone. To the solution, formic acid was added in various concentrations. The solution was loaded into an autoclave and the hydrothermal reaction was carried at 200 °C for 24 h with a heating rate of 5 °C/min. The obtained powders were centrifuged, washed and dried in air at 60 °C for 12 h, then calcined at 900 °C for 2 h. As mentioned before, nanoparticles are beneficial to the transport of Li^+ ions. Micro-sized spheres are also relevant for the application as an anode material because they provide good mechanical stress relief upon lithium insertion/extraction (NOH; CHOI, 2016).

Choi et al. (2017) studied the kinetics of solid state reaction $TiO_2 + Nb_2O_5 \longrightarrow TiNb_2O_7$. They found that Nb-rich phases form at a first moment, followed by the complex oxide formation pathway $TiNb_{24}O_{62} \longrightarrow Ti_2Nb_{10}O_{29} \longrightarrow TiNb_2O_7$. A simple first-order model was proposed and the reaction rate constant and activation energy were calculated.

Liu, Liu, et al. (2017) synthesized Ag-coated TNO by a solid state reaction followed by a solvothermal process for the coating. TiO_2 and Nb_2O_5 were mixed in a planetary ball mill for 6 h and then calcined at 1100 °C for 24 h. The as-synthesized TNO was thereafter mixed with $AgNO_3$ and polyvinylpyrrolidone in N,N-dimethylformamide and ultrasonicated for 30 min. The mixture was transferred to an autoclave and kept at 160 °C for 1 h. The final product was washed and dried to obtain TNO microcrystals coated by Ag nanoparticles. When applied as an anode, the 2nd discharge was $275.3 \, \text{mAh g}^{-1}$ at 1 C, compared to $234.2 \, \text{mAh g}^{-1}$ for pure TNO. The rate capability was also improved compared to pristine TNO and thus the coating was said to be an effective method to improve the electronic conductivity of the material.

Lou, Cheng, et al. (2017) synthesized ordered macroporous $TiNb_2O_7$ made of nanoparticles. They used monodispersed polystyrene (PS) as hard templates for the generation of porosity. The precursor solution was obtained by mixing titanium (IV) butoxide and niobium (V) chloride in ethanol. PS colloidal crystals were soaked in the precursor for 12 h then vacuum filtration was used to remove excess of solution. The samples were dried and PS removed by calcination in air at 900 °C for 5 h with a heating rate of 1 °C/min. The material exhibited rate capability of $120 \, \text{mAh g}^{-1}$ at 50 C and 82 % capacity retention over 1000 cycles at 10 C.

Pham-Cong et al. (2017) synthesized molibdenium sulfide-coated TNO nanofibers by electrospinning method with the reaction being carried via sol-gel method. The starting materials were niobium(V) ethoxide and titanium(IV) butoxide. PVP was used an as additive. The fibers were made of serially interconnected nanograins with diameter of ~200 nm.

Haoxiang Yu et al. (2017) prepared one-dimensional TNO hollow fibers by one-step dual-nozzle coaxial coelectrospinning, followed by calcination. The outer sol solution was prepared by mixing polyvinylpyrrodidone, ethanol and N,N-dimethylformamide with a solution containing titanium(IV) butoxide, niobium(V) ethoxide, ethanol, N,N-dimethylformamide and acetic acid. The inner sol solution was prepared by mixing poly(acrylonitrile) with N,N-dimethylformamide. After electrospinning, the precursor fibers were calcined in air at 800 °C for 9 h with a heating rate of 3 °C/min to obtain TNO hollow nanofibers. These fibers had a outer diameter of 220 nm and wall thickness of 60 nm.

Zhuobin Yu et al. (2017) studied the photocatalytic activity of TNO and synthesized it via a hydrothermal reaction. They mixed niobium oxalate and titanium oxysulfate

in KOH solution. The solution was transferred to an autoclave and kept at 180 °C for 24 h. The obtained white precipitate was separated by centrifugation, washed and dried at 80 °C for 12 h. The samples was then calcined in air for 700 °C for 3 h with a heating rate of 5 °C/min. They also treated the samples in ammonia gas to dope the material with nitrogen.

Ise et al. (2018) synthesized TNO nanoparticles via a hydrothermal reaction and compared to TNO synthesized via solid state method. For hydrothermal reaction, they mixed titanium chloride dissolved in sulfuric acid with niobium chloride dissolved in ethanol. Ammonia solution was added to adjust the pH. The mixture was transferred to an autoclave and maintained at 160 °C for 5 h. The amorphous solid was separated by freeze-drying under vacuum, then calcined at 1000 °C for 30 min. For the solid state method, they mixed anatase TiO_2 with $Nb(OH)_5$ in a planetary ball mill. The mixture was then calcined at 1100 °C for 12 h. The primary particle sizes of the hydrothermally prepared TNO were 50–300 nm. For the solid state approach, the particle sizes were 0.5–1 μm.

Jiao et al. (2018) synthesized holey graphene-supported nanostructured TNO via hydrothermal method and annealing treatment. Holey-graphene oxide dispersed in ethanol was mixed with $NbCl_5$ and titanium butoxide. A solution of oleylamine in ethanol was added dropwise. The mixture was transferred to an autoclave and maintained at 200 °C for 24 h. The products were centrifuged, washed with ethanol and water to remove oleylamine and ions and thereafter freeze-dried. The material was then annealed at 900 °C for 2 h in N_2 atmosphere.

Liu, Zhao, et al. (2018) synthesized TNO microspheres with a mesoporous structure by a solvothermal reaction. Titanium(IV) isopropoxide and niobium(V) chloride were added to a mixture of glycerol and isopropanol. The solution was transferred to an autoclave and the reaction was carried at 180 °C for 24 h. The precipitate was separated and then calcined at 750 °C in air for 12 h. They also prepared TNO via solid state reaction, which did not form mesopores, by mixing TiO_2 and Nb_2O_5 in ball mill and then calcining at 1100 °C for 24 h. The subunit size was 50 nm with a crystalline size of 17 nm and the diameter of the microspheres was 0.6–0.9 μm. An initial capacity of 319 mAhg^{-1} was achieved at 0.1 C and high rate capacity of 155 mAhg^{-1} at 1 C and 10 C. Capacity fading was only 0.03 % per cycle after 500 cycles at 10 C.

Takami et al. (2018) studied the use of TNO as an anode in LIBs for automotive applications. They synthesized TNO via a solid state reaction, by mixing TiO_2 and $Nb(OH)_5$ in a planetary ball mill, followed by calcination at 1100 °C for 12 h. The TNO powder was mixed with an aqueous solution of disaccharide and the mixture was spray-dried to produce microspheres. The secondary spherical particles had particle sizes in the range 50–20 μm. They were heated at 700 °C in argon atmosphere for carbon coating.

Yoon et al. (2018) synthesized dual-phase $Nb_2O_5/TiNb_2O_7$ with carbon coating via a solvothermal reaction. The starting materials were niobium(V) chloride and titanium isopropoxide, which were dissolved in ethanol and transferred into an autoclave. The solvothermal reaction was carried at 180 °C for 24 h with a heating/cooling rate of 2 °C/min. The obtained powder was separated and heated at 700 °C for 2 h. The carbon coating was achieved by hydrothermal reaction with an aqueous solution of glucose at 180 °C for 12 h. The product was separated by centrifugation and calcined at 700 °C for 1 h under Ar flow. A surface area of $34.5\,m^2 g^{-1}$ was obtained for the carbon-coated microspheres.

Li et al. (2019) synthesized TNO nanowires by using sulfonated poly(DVB-co-VBC) nanotubes (SPNTs) via a sol-gel procedure. The SPNTs were dispersed in ethanol to which titanium butoxide was added and stirred for 6 h. Niobium chloride dissolved in ethanol was added and the reaction mixture was further stirred at 60 °C for 4 h. The precursor was separated by centrigufation, then dried and calcined in air at 800 °C for 5 h with a heating rate of 2 °C/min.

Luo et al. (2020) synthesized activated carbon cloth at $TiNb_2O_7$ (ACC@TNO) "like stab grown on the thorn" via a hydrothermal reaction and subsequent calcination. Titanium butoxide and niobium(V) chloride were mixed in alcohol, to which activated carbon cloth is added and stirred for 1 h. The mixture was then hydrothermally treated at 180 °C for 24 h. The precursor was separated and calcined at 900 °C for 5 h with heating rate of 2 °C/min in Ar atmosphere.

In summary, one may notice that historically works that employed a solid state method are outnumbered by works relying on Ti^{4+} and Nb^{5+} precursors and lower temperature reactions (sol-gel, solvothermal, hydrothermal) followed by calcination to form TNO. This is mainly due to the possibility of tailoring microstructure for the latter - both in a matter of shape and of size -, which is indeed a dictating factor of electrochemical performance besides the exploitation of secondary species (doping, coating etc). Nevertheless, as Choi et al. (2017) points out, for the large scale production of $TiNb_2O_7$, the solid state route is still appealing due to its simplicity, cost-effectiveness and consequent scalability. However, one may also notice that the time employed in the works related to the solid state method are on the scale of tens of hours. In this work, we propose a much more efficient approach to synthesizing TNO via a solid state reaction on the scale of minutes: *fast firing*. In Figure 2, one sees a comparison between the time-temperature cycle used in the current work compared to other works. This seems to be the first time $TiNb_2O_7$ is synthesized in such a short time using a solid state reaction.

Figure 2 – Comparison of the temperature-time employed to synthesize $TiNb_2O_7$ in this work and other works
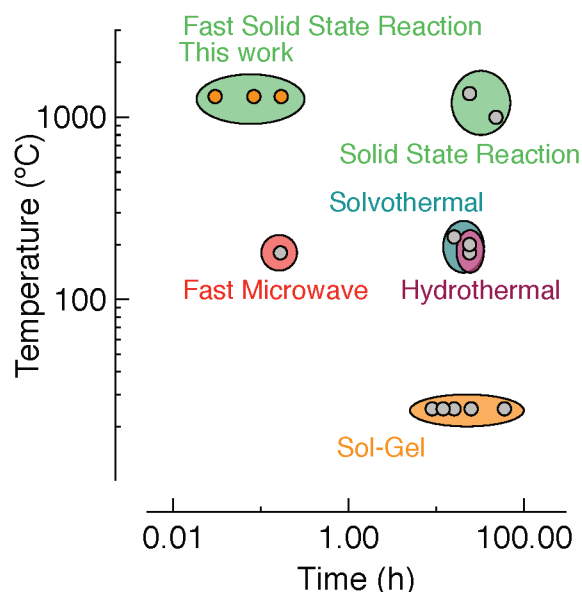
Source: adapted from Falk, Rodrigues Neto, et al. (2019)

2.2 TAPE CASTING

Tape casting is a ceramic forming technique to produce thin flat sheets. It is based on the flow of a suspension down a reservoir and under a *blade* which is only a fraction of a millimeter from the bottom substrate. The main apparatus contains a blade, named the *doctor blade*, and a reservoir. The entire equipment including a moving substrate is known as a tape caster. The flow is guaranteed both by the gravitational head in the reservoir and the shear effect of the moving substrate (MISTLER; TWINAME, 2000). The thickness of the tape, which is the primarily controlled parameter, is determined by the blade gap (blade height) and the cited driving forces of fluid flow. The pressure gradient in the doctor blade region is also affected by the overall geometry of the equipment, including the blade width and the dimensions of the reservoir. A schematic is shown in Figure 3.

Figure 3 – Schematic of a tape casting machine
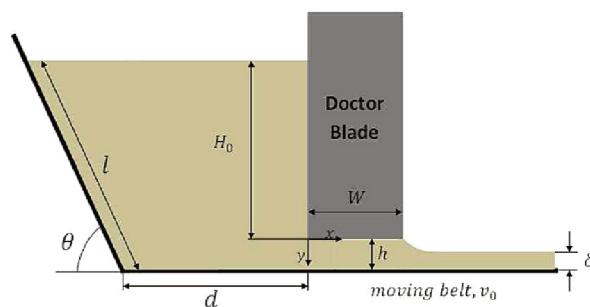
Source: Jabbari et al. (2016)

The process was initially developed in the 1940s to produce mica capacitors and was shortly after made public in an article by Howatt, Breckenridge, and Brownlow (1947). The main application is still today the fabrication of ceramic capacitors, although exploration to develop solid-oxide fuel cells and filtration membranes is ongoing since the last decades.

Tape casting relies on a set of ingredients that make up the initial ceramic slurry. They are the powder, the solvent and the so-called additives: binder, dispersant and plasticizer (and often other sorts of additives such a defoamer, which is used in this work). The powder is the major ingredient and mainly determines the properties of the final material - since the solvent is evaporated and the additives burned off in the subsequent steps of processing. The solvent serves as a vehicle for all the ingredients, dispersing or dissolving them, guaranteeing a homogeneous slurry and providing a mechanism for flow under the casting blade (flowability). In the industry, the most typical solvents are organic, yet significant research has been done in the last decades for aqueous systems, which are advantageous because of the availability, low cost, non-toxicity, non-flammability and environmental friendliness of water. The main drawback is the high heat of vaporization of water, which impairs the drying operation in terms of energy cost (MISTLER; TWINAME, 2000). Concerning the additives, the binder affects both the slurry rheology and creates a body-spanning network of particles in the green tape, allowing it to be handled without breaking. The plasticizer *softens* the binder and enhances mechanical properties such as plasticity and flexibility and inhibits crack formation. The anti-foaming agent or defoamer is used to prevent foaming after the agitation of the slurry.

2.3 RHEOLOGY

The field of fluid rheology and in particular particle suspensions owes its maturity and richness to its applicability in several industries and areas of research, including foodstuff, cosmetics, plastics, pharmaceutical, oil and mineral separation (MUELLER;

LLEWELLIN; MADER, 2010). The main aspect of rheology theory is to describe how complex fluids deform responding to an applied shear or tensile stress.

One of the idealizations that are first presented when discussing the subject is that of the Newtonian fluid, which presents a linear relationship between the applied shear stress and the strain rate,

$$\tau = \eta \dot{\gamma} \tag{1}$$

Equation (1) not only serves to define a Newtonian fluid, but it also defines what is known as the apparent viscosity η: the ratio $\tau/\dot{\gamma}$, which is used to describe all rheological behaviours. When the apparent viscosity is dependent on the strain rate, the fluid is called non-Newtonian. Another relevant case is when the apparent viscosity is a function of time for a constant strain rate, temperature and composition. In this scenario, if η decreases over time, the fluid is said to be thixotropic, whilst if η increases over time, which is rarer, the fluid is rheopectic.

2.3.1 Non-Newtonian fluids

The viscosity of complex fluids is generally dependent on the applied shear stress or strain rate. Figure 4 displays the different possible behaviours, namely Newtonian: the relationship between shear stress and strain rate is linear; shear-thickening (or dilatant): the apparent viscosity increases with the shear rate; shear-thinning (or pseudoplastic): the apparent viscosity decreases with the shear rate; Bingham plastic and plastic: the fluid presents a *yield stress* and will only start deforming continuously above a certain stress value.

Figure 4 – Different rheological behaviours

$\dot{\gamma}$ (Shear rate)
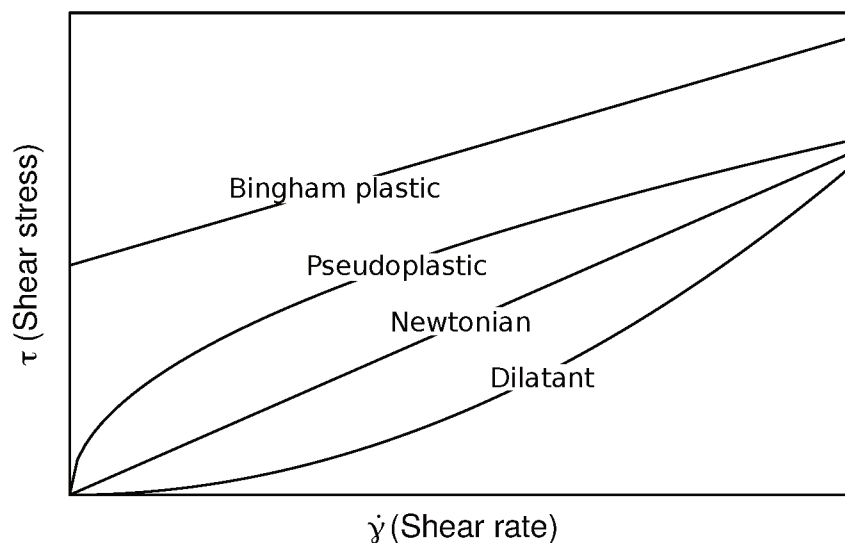
A general equation to describe non-Newtonian fluids is

$$\tau = \tau_0 + k\dot{\gamma}^n \tag{2}$$

Where τ_0 is the yield stress; k, the flow consistency index; and n, the flow behaviour index. A particular version of Equation (2) is the Ostwald power-law model, when the yield stress reduces to zero,

$$\tau = k\dot{\gamma}^n \tag{3}$$

Shear-thinning (pseudoplastic) behaviour is observed whenever $n < 1$ in Equation (3), which is an interesting particular case when it comes to tape casting, as one wishes to guarantee flow in the high-shear region - the doctor blade region - but at the same time maintain shape in the wet tape after casting.

2.3.2   Viscosity of suspensions

Suspensions of spherical particles at low solids volume fraction (ϕ) have their viscosity increased linearly with ϕ as shown by Einstein (1906),

$$\eta = \mu(1 + 2.5\phi) \tag{4}$$

Arrhenius made the argument that the Einstein relation (Equation (4)) could be extended by pretending an increment $d\eta$ is created in a suspension with a corresponding infinitesimal increase in particle fraction,

$$d\eta = 2.5\eta(\phi)d\phi \tag{5}$$

This can be integrated to give

$$\eta = \mu \exp(2.5\phi) \tag{6}$$

Larson (1999) argues that Equation (6) can be extended for non-spherical particles by tuning the numerical coefficient in the relation, therefore

$$\eta = \mu \exp([\eta]\phi) \tag{7}$$

with $[\eta] = 2.5$ being valid for spherical particles. $[\eta]$ is called the intrinsic viscosity and can be mathematically defined as

$$[\eta] = \lim_{\phi \to 0} \frac{\eta - \mu}{\phi\mu} \tag{8}$$

As the solid fraction is increased, the maximum solid fraction can be achieved where the particles come in contact with each other and form a packed bed. Equation (7) must then be corrected to (LARSON, 1999),

$$\eta = \mu \left(1 - \frac{\phi}{\phi_m} \right)^{-[\eta]\phi_m} \tag{9}$$

Where ϕ_m is the maximal volume fraction (0.64 for hard spheres). For particle loading in the range $\phi > 0.3$, viscosity becomes sensitive to strain rate, i.e. the fluid is no longer Newtonian (LARSON, 1999).

2.4 SINTERING

Sintering is the transformation of a powder system into a solid body by the application of thermal energy. The method has been used for millennia to fire pottery and metals. Today, all ceramic processing routes include some kind of sintering step.

The driving force for sintering is the reduction of total surface energy, which can be expressed as

$$d(\gamma A) = d\gamma A + \gamma dA \tag{10}$$

Generally, the reduction in surface energy γ is due to the exchange of solid-vapour interface to a solid-solid interface and is attributed to densification, while the change in area A is due to grain growth. The variables in sintering are geometric such as particle shape and size (and distribution) and state of agglomeration; process-related, like temperature, time and pressure; and chemical, like composition and homogeneity.

There are three stages of solid state sintering. The initial phase is characterised by the formation of necks between the particles and is limited to 2-3% of shrinkage. During the second stage, the majority of densification (up to 93%) occurs, until isolated pores appear. In the final stage, the isolated pores close and full densification is achieved (KANG, 2005).

Fast firing is a sintering technique in which the ceramic body experiences a high heating rate and a short total sintering cycle. It was first proposed by Harmer and Brook (1981) as a method to mitigate grain growth in favor of densification. Fast firing can be used whenever the activation energy of densification is higher than that of grain growth (KANG, 2005). It is also an advantageous method when it comes to energy savings and productivity since a similar product can be manufactured at a shorter total furnace time.

2.5 COLLOIDAL STABILITY

Colloids are particle systems whose entities have some dimension between 1 nm and 1 µm (HIEMENZ; RAJAGOPALAN, 1997). The powders used in this work lie close to the upper part of this range. Colloidal dispersions are two-phase systems including a continuous and a dispersed phase. They do not easily separate by gravitational settling, although centrifuging may be applied for this purpose. In the case of ceramic suspensions of small particles, the continuous phase is the liquid (the solvent and dissolved additives) and the dispersed phase are the solid particles or aggregates thereof.

Small particles in a colloidal dispersion tend to exist as aggregates or groups of particles that are clumped and move together as if they were single particles. The formation of larger aggregates leads to sedimentation, as suggested by Stokes's law, where the steady-state settling velocity increases with the hydraulic radius,

$$v = \frac{2}{9} \frac{R_h^2 \Delta \rho g}{\eta}. \tag{11}$$

Where $\Delta \rho$ is the density difference between the particle and the fluid; η, the dynamic viscosity; R_h, the hydraulic radius; g, the acceleration of gravity; and v, the settling velocity.

Colloidal stability refers to the prevention of aggregation and thus of sedimentation. There are essentially two mechanisms of stability: electrostatic repulsion and steric effect. In electrostatic repulsion, the charges at the particle surface repel each other by simple Coulombic interaction. This can be amplified by the use of surface-active molecules (or surfactants) that adsorb onto the particles and provide charges by ionic dissociation of certain groups along the molecular chain. The other mechanism, the steric effect, is also accomplished by a surfactant, though in this case the molecules are long and entangled hence providing a mechanical repulsion among the particles. The combination of both mechanisms is called the electrosteric effect.

Zeta potential is the electric potential at the shear plane around the particles, where the liquid velocity is zero. This does not coincide with the particle surface itself but with the outer surface level of ions attached to the particles by electrostatic attraction. The zeta potential is a key indicator of colloidal stability and is higher in absolute value for stable dispersions. A value greater than 30 mV or lower than –30 mV is generally associated with good stability.

3 MATERIALS AND METHODS

3.1 SAMPLE PREPARATION

The suspensions are prepared by initially adding dispersant dropwise into deionized water in a 50 mL Falcon tube. To the water-dispersant mixture, TiO_2 (Anatase 1171 Kronos, $d_{50} = 0.26\,\mu m$) and Nb_2O_5 (GO 350, optical degree, $d_{50} = 0.967\,\mu m$, supplied by Companhia Brasileira de Metalurgia e Mineração - CBMM) are separately added. The total mass of powder was set as 22 g for each sample, which is processed into a single tape. 44 g of inert zirconia balls with a diameter of 5 mm are added and the suspension is put on a ball mill for 24 h. After that, the binder, plasticizer and defoamer (and co-surfactant for some samples) are added and the slurry is ball milled again for 1 h. The slurry is then sieved to separate the zirconia balls and rests for 2 h to eliminate air bubbles. It is then cast using a doctor blade height of 0.58 mm over the substrate of biaxially-oriented polyethylene terephthalate (BoPET), commercially called Mylar® (specifically Mylar G10JRM, Mistler), structure shown in Figure 5. Although one side of Mylar® is silicone-coated, the other side is chosen to cast the suspension for a wettability reason - the silicone-coated side is more hydrophobic and thus an aqueous suspension does not spread evenly on it. The tape casting machine (or tape caster) used was CC-1200, Mistler with a belt speed of $2\,mm\,s^{-1}$.

Figure 5 – Polyethylene terephthalate chemical structure
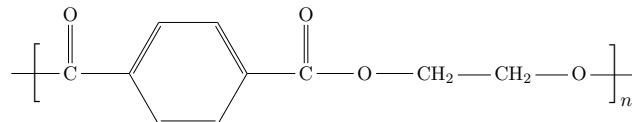
The wet tape is thereafter dried for 24 h at room temperature and humidity level (neither are strictly controlled in these experiments). The dry tape is cut in 3×3 cm pieces and put inside the furnace in air atmosphere. The temperature cycle for conventionally sintered tapes is given in Figure 6. The initial heating rate is set to 1 °C/min, until the debinding temperature of 500 °C is achieved, which is held for 1 h. The second heating rate is 5 °C/min. The final target temperature is 1280 °C, which is held for 2 h, after which the tapes are cooled down to room temperature and removed from the furnace. The slurry preparation process, formulation and furnace cycles for conventionally sintered tapes are based on the work of Moreno, Aguilar, and Hotza (2012), with some modifications.

The fast-fired tapes are processed similarly, though calcination is performed in two steps. The tapes are first heated to 600 °C to burn off additives in a heating rate of 1 °C/min and a holding time at that temperature of 1 h. The tapes are cooled to room temperature and then placed inside the fast firing furnace which is already heated to
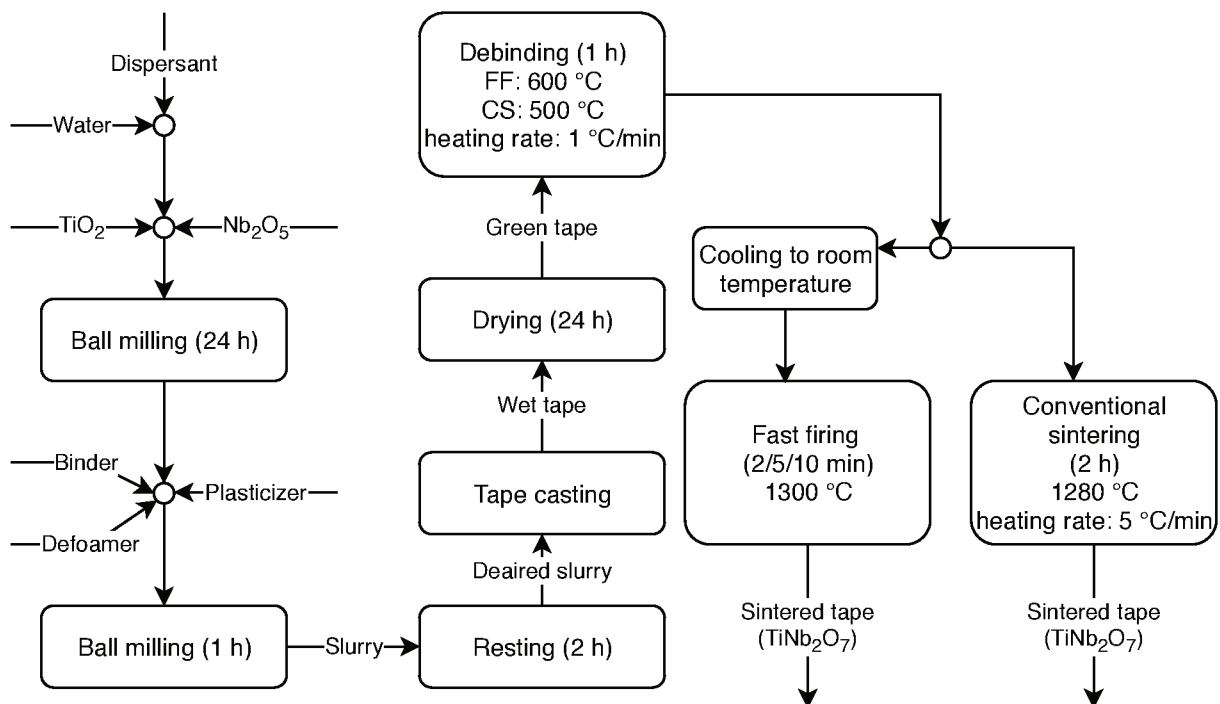
1300 °C. Different samples were prepared by changing the holding time in the fast firing step, namely 2 min, 5 min and 10 min (labeled FF2, FF5 and FF10 respectively).

Figure 6 – Furnace cycle for conventionally sintered tapes
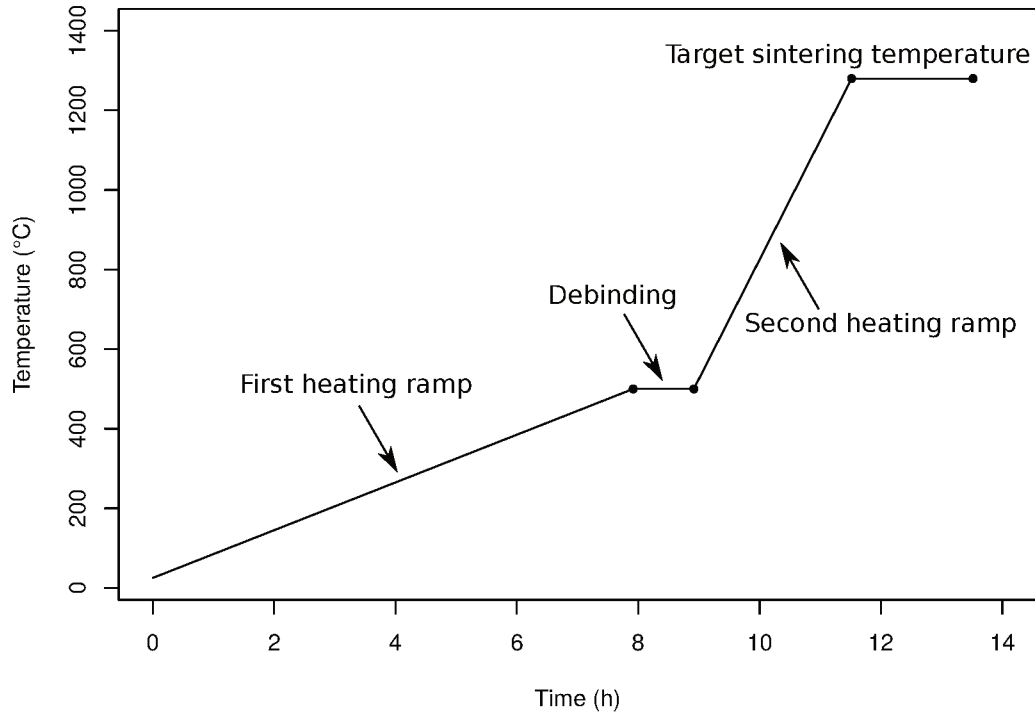
A scheme of the process is shown in Figure 7.

Figure 7 – Tape preparation process

3.2 MATERIALS

3.2.1 Amount of powders

The TiO_2 and Nb_2O_5 powders are added separately at each sample preparation step. They respect a 1:1 molar ratio to favour the formation of the $TiNb_2O_7$ phase during sintering, according to the stoichiometry of the balanced equation $TiO_2 + Nb_2O_5 \longrightarrow TiNb_2O_7$. This corresponds to a 23.10 wt.% of TiO_2 and 76.90 wt.% of Nb_2O_5, which are calculated from the conversion of molar to mass fraction, given by

$$\omega_{TiO_2} = \frac{x_{TiO_2}M_{TiO_2}}{x_{TiO_2}M_{TiO_2} + x_{Nb_2O_5}M_{Nb_2O_5}} = \frac{0.5 \times 79.866}{0.5 \times 79.866 + 0.5 \times 265.81} = 0.2310 \quad (12)$$

Where ω is the mass fraction with respect to the TiO_2-Nb_2O_5 system, x is the corresponding molar fraction and M is the molar mass.

3.2.2 Amount of water

Water is used as a solvent and is added according to the volume fraction of solids, also called the solids loading.

$$\phi = \frac{\text{Volume of solids}}{\text{Volume of water + Volume of solids}} \quad (13)$$

For 30 vol.% used in some slurries in this work (see Table 1 in subsection 3.2.3), the mass fraction of solids with respect to the water + solids basis is

$$\omega_S = \frac{\phi\rho_S}{\phi\rho_S + (1-\phi)\rho_W} = \frac{0.3 \times 4.2}{0.3 \times 4.2 + 0.7 \times 1.0} = 0.65 \quad (14)$$

where ρ_S is the powder density and ρ_W is the water density. ϕ is the volume fraction of solids (solids loading). ρ_S is calculated by the weighted average of the inverses of the densities of TiO_2 and Nb_2O_5,

$$\rho_S = (\omega_{TiO_2}\rho_{TiO_2}^{-1} + \omega_{Nb_2O_5}\rho_{Nb_2O_5}^{-1})^{-1} = (0.231 \times 3.8^{-1} + 0.769 \times 4.4^{-1})^{-1} = 4.2\,\text{g}\,\text{cm}^{-3} \quad (15)$$

where $\rho_{TiO_2} = 3.8\,\text{g}\,\text{cm}^{-3}$ is the real density of the titania powder and $\rho_{Nb_2O_5} = 4.4\,\text{g}\,\text{cm}^{-3}$ is the real density of the niobia powder. ω_{TiO_2} and $\omega_{Nb_2O_5}$ were calculated in Equation (12).

3.2.3 Additives

The additives are added to the suspension according to a ratio of the mass of additive per mass of solids, expressed as a percentage.

$$\%\text{Additive} = \frac{\text{Mass of additive}}{\text{Mass of solids}} \quad (16)$$

All additives are (mixtures of) organic compounds and thus are burned off during the thermal treatment (debinding). They nonetheless affect the stability with respect to agglomeration and sedimentation, the rheological properties of the suspension and mechanical aspects of the green tape such as plasticity and flexibility. They are also key to the prevention of crack formation during the final stages of drying.

The binder is an acrylic polymer emulsion (Mowilith® LDM 6138). The dispersant is ammonium polymethacrylate (Darvan® C-N, structure shown in Figure 8). The defoamer is an aqueous silicone emulsion (Antifoam Y-30® Emulsion). The plasticizer is polyethylene glycol (M_W = 1500 g/mol), whose structure is shown in Figure 9. The co-surfactant is cocamide DEA, a mixture of diethanolamides of coconut oil fatty acids.
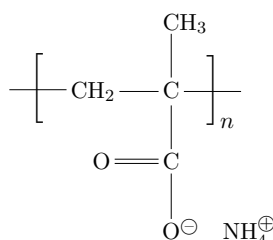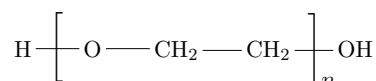
Figure 8 – Ammonium polymethacrylate chemical structure

Figure 9 – Polyethylene glycol chemical structure

The slurries discussed in this text are labeled A, B, C, D, E and F. Their compositions are given in Table 1. All fast fired tapes were prepared from slurry A, as well as some conventionally sintered tapes. This formulation (A), which was deemed optimal for our objectives, did not include a co-surfactant (cocamide DEA) as it was found that the process could be unfolded in its absence with no compromise. Slurries D, E and F were prepared to test the effect of solids loading on the rheological behaviour, as they are prepared with solids loadings of 45 vol.%, 35 vol % and 30 vol.% respectively. Slurry C is used to compare the presence of cracks with slurry A, which presented no crack formation after drying due to the inclusion of a plasticizer. Contact angle measurements were done with a conventionally sintered tape from slurry B.

Table 1 – Compositions of the slurries discussed in this text

Ingredient	A	B	C	D	E	F
Solids (vol.%)	30.04	27.40	39.98	45.04	35.01	29.94
Dispersant (wt.%)	1.91	1.42	2.00	2.05	1.80	1.94
Binder (wt.%)	24.68	25.56	35.28	24.70	25.06	25.92
Co-surfactant (wt.%)	-	1.75	1.68	0.85	1.00	1.20
Defoamer (wt.%)	0.27	0.67	0.48	0.60	0.45	0.40
Plasticizer (wt.%)	22.50	-	-	-	-	-

3.3 ANALYSIS AND MEASUREMENTS

The analysis/measurements with the corresponding equipment employed in this work are shown in Table 2 with the column Material describing which material step (powder, slurry, green tape and sintered tape) they refer to.

For zeta potential and average particle size titrations, separate suspensions of TiO_2 (5.77 g) and Nb_2O_5 (19.22 g) were prepared in deionized water (3.17 g of water for TiO_2 and 10.56 g for Nb_2O_5), each with 2 wt.% of dispersant (Darvan® C-N) – adding these two suspensions yields a slurry with ϕ = 30 vol.%, though they were analysed separately. After ball milling for 24 h, a droplet of each suspension was transfered to separate 50 ml Falcon tubes. The tubes were then filled with deionized water for dilution (the mass of water added was ~100× the mass of the droplet), which concluded the sample preparation for the analysis.

For rheological measurements, a polished parallel disc geometry with a diameter of 60 mm was used with a gap of 0.15 mm.

For TGA and DTG, the heating rate during the entire analysis was 5 °C/min and it was conducted under synthetic air (5.0, 99.999 % purity) atmosphere.

For the frequency-dependent dielectric measurement, a commercial setup was used (test fixture Agilent 16451B) at a voltage of 1 V and the tested frequency range was 20 Hz–2 MHz. The dielectric constants of fast-fired tapes FF2 and FF5 were not measured because the samples exhibited fragility upon the mechanical pressure exerted during the test.

XRD analysis was conducted with CuKα radiation at 40 kV and 15 mA. Angular step was 0.05° with step time of 1 s.

To calculate the average grain size of fast-fired tapes from SEM images, 20 grains with discernible grain boundaries were chosen across the image and their diameter were measured, then the arithmetic mean was calculated. For the conventionally sintered tape, since a near primatic shape was observed, the average of the longitudinal and radial lengths were taken for 10 grains, which were then averaged.

Contact angle was not measured for fast-fired tapes because the water droplet quickly penetrated the structure because of their high open porosities.

Table 2 – Analytical methods/measurements and the corresponding equipment used in this work

Analysis	Equipment	Material
Average particle size	Malvern Zetasizer Nanosizer with MPT-2 Autotitrator, DLS at 173°	Powder
Zeta potential	Malvern Zetasizer Nanosizer with MPT-2 Autotitrator	Powder
Rheology	Thermo Scientific Haake Mars II rheometer, Thermo Fisher Scientific	Slurry
pH	AZ pHmeter 86505	Slurry
TGA	STA 449 F3 Jupiter, Netzsch	Green tape
Contact angle	ramé-hart Model 250	Sintered tape
Porosity and density	Archimedes apparatus	Sintered tape
Real density	Micromeritics AccuPyc II 1340 Gas Pycnometer	Sintered tape
XRD	MiniFlex600, Rigaku	Sintered tape & powder
SEM	Hitachi, TM 3030	Sintered tape
Dielectric constant	Agilent E4980A LCR precision meter with test fixture Agilent 16451B	Sintered tape

The Archimedes method for measuring porosity and density was used according to the ASTM C 20 (2000) norm. A sample (or tape in this work) is weighed as a dry piece (m_{dry}) and then immersed in water for 24 h and weighed again (m_{wet}). After that, an apparatus is set where the sample is weighed while immersed in the water ($m_{immersed}$). The open or apparent porosity is

$$\varepsilon_{open} = \frac{m_{wet} - m_{dry}}{m_{wet} - m_{immersed}} \tag{17}$$

The bulk density (ρ_{bulk}) is related to the water density (ρ_W) as

$$\rho_{bulk} = \frac{m_{dry}}{m_{wet} - m_{immersed}} \rho_W \tag{18}$$

The total porosity is

$$\varepsilon_{total} = \frac{\rho_{real} - \rho_{bulk}}{\rho_{real}} \tag{19}$$

Where $\rho_{real} = \rho_{TiNb_2O_7}$ is the real or true density of the material.

4 RESULTS AND DISCUSSION

4.1 STARTING MATERIALS

Starting materials (TiO_2 and Nb_2O_5) were characterised in terms of XRD patterns, zeta potential titration and average particle size titration.

The XRD patterns for TiO_2 and Nb_2O_5 are shown in Figures 10 and 11 respectively. The TiO_2 crystals consist of a pure anatase phase compatible with JCPDS no. 01-084-1286. The Nb_2O_5 particles are comprised of mixed orthorhombic (JCPDS no. 00-030-0873) and monoclinic (JCPDS no. 00-016-0053) phases. This result confirms purity as well as crystallinity of the starting materials.

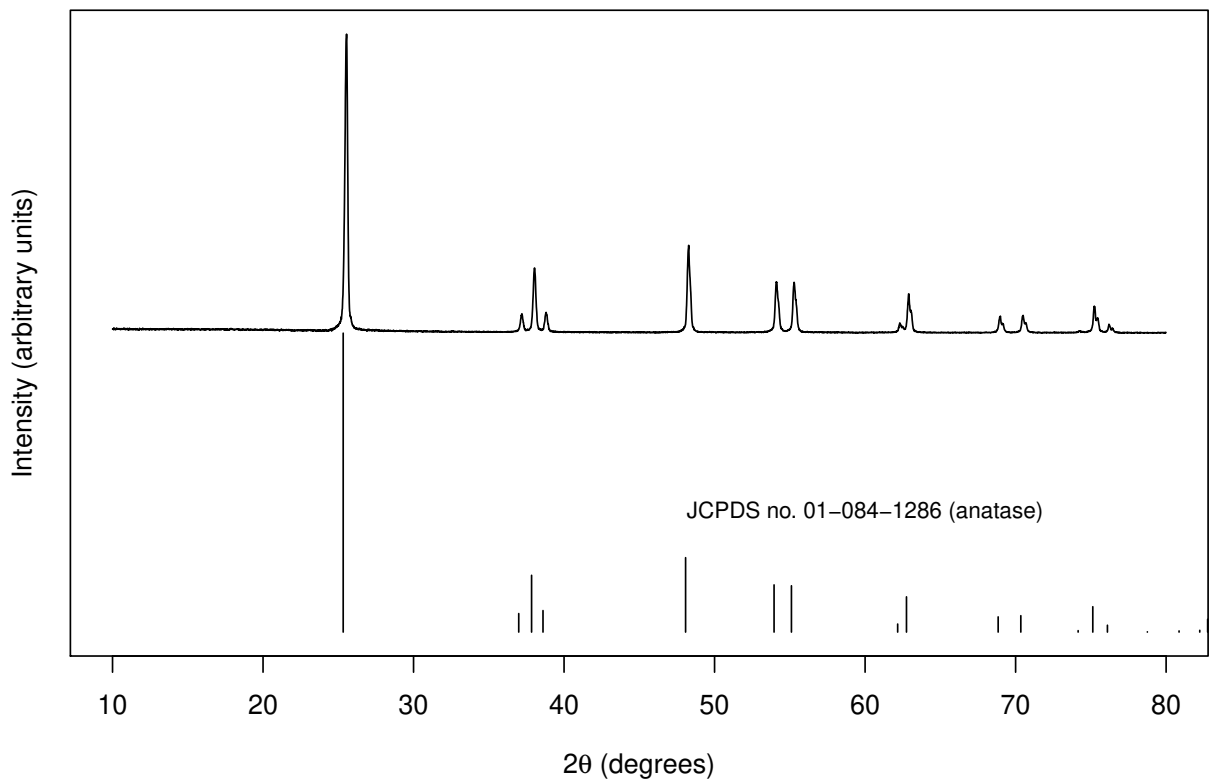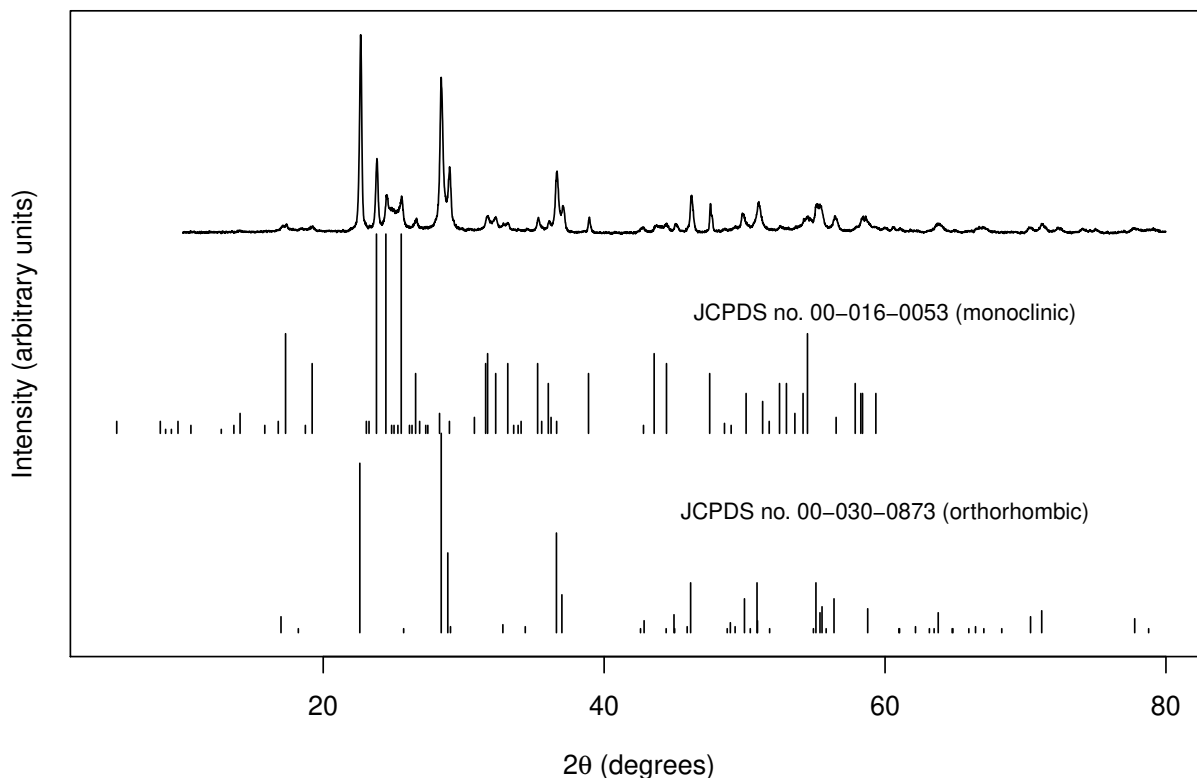Figure 10 – XRD Pattern of the TiO_2 powder (pure anatase phase)

Figure 11 – XRD Pattern of the Nb_2O_5 powder (mixed orthorhombic and monoclinic phases)

Zeta potential as a function of pH is shown in Figure 12 for both titania and niobia powders dispersed in water with dispersant Darvan® C-N (2 wt.%). The measured isoelectric point was 4.21 for Nb_2O_5 and 5.30 for TiO_2. The suspension at a solids loading of 30 vol.% has pH = 6, in which the zeta potential is near the isoelectric point for TiO_2 and ~ −30 mV for Nb_2O_5. This translates to good stability for the latter and poor stability for the former, which could lead to homoagglomeration of TiO_2 particles although it probably prevents heteroagglomeration. However, the suspension proved stable throughout the time of processing, given it is cast right after ball milling, rests for only 2 h to eliminate air bubbles and is dried afterwards. It might be the case that the dispersant (Darvan® CN) does not interact well with the TiO_2 particles thus not supplying a mechanism for stability. The entire system stability could in prospect be enhanced nevertheless by the addition of a strong base solution (e.g. NaOH). However, that could lead to some processing problems at very high pH levels - for example, related to corrosion.

The titration curve of average particle size versus pH is shown in Figure 13 for the same systems as in the zeta potential titration. The measured average particle sizes are coarser than the median particle size provided by the suppliers, $d_{50} = 0.26\,\mu m$ for TiO_2 and $d_{50} = 0.967\,\mu m$ for Nb_2O_5 (and also larger than the grain sizes seen in SEM images for fast-fired tapes in Figure 19 later in this chapter). Indeed, at the isoelectric

point the surface charges are neutral thus leading to easy agglomeration of particles. This can be observed at the maximum average particle size in Figure 13, which is near the isoelectric point for Nb_2O_5. For TiO_2 the absence of this maximum is in agreement with the low variation of the zeta potential for the wide pH range.

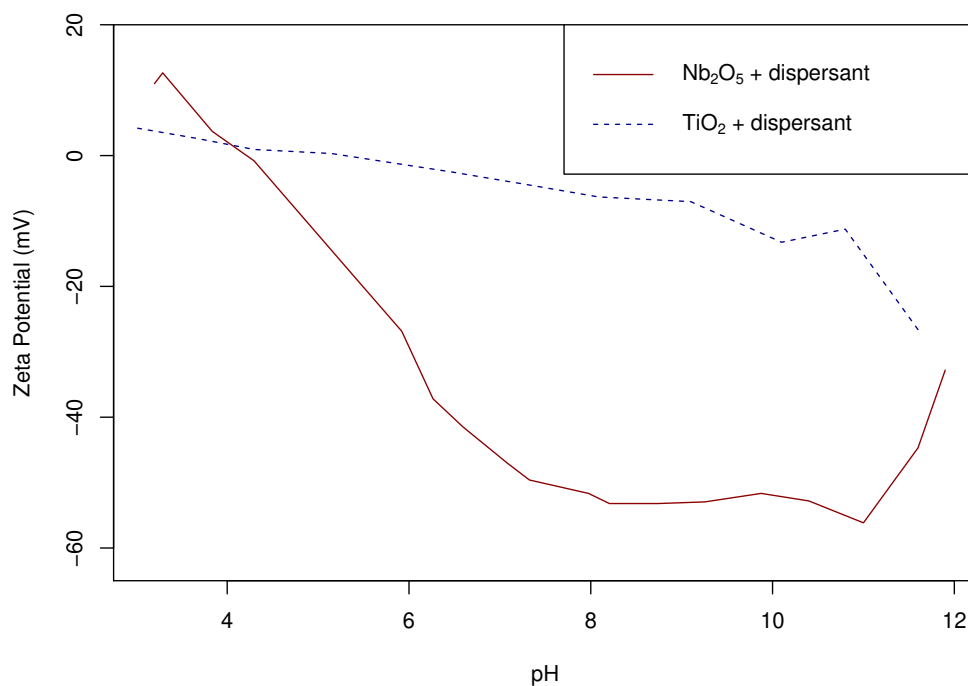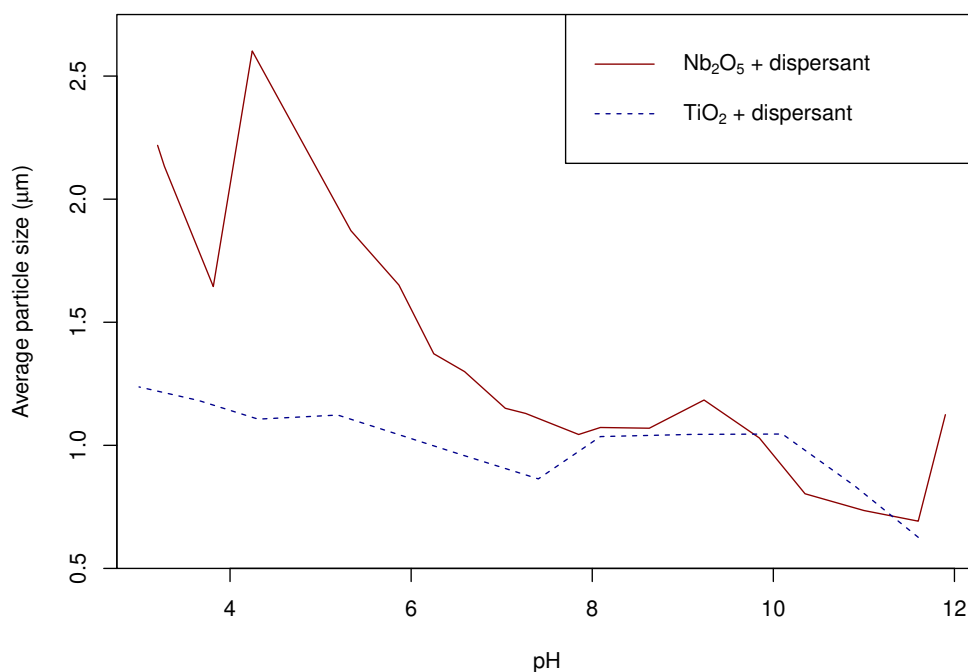Figure 12 – Zeta potential versus pH for TiO_2 suspension with dispersant and Nb_2O_5 suspension with dispersant

Figure 13 – Average particle size versus pH for TiO_2 suspension with dispersant and Nb_2O_5 suspension with dispersant

4.2   SLURRY AND GREEN TAPE

Slurries were characterised in terms of their rheology by constructing the shear stress versus strain rate curves for different solids loadings. The comparison is shown in Figure 14. The dynamic viscosity of the suspensions as a function of strain rate is also shown in Figure 15. Rheological data were fitted to a power-law model (Equation (3) in subsection 2.3.1). Calculated coefficients are presented in Table 3, with high R^2 values indicating adequacy of the model. All rheological curves in the tested samples ($\phi = 30$ vol.%, 35 vol.% and 45 vol.%) showed pseudoplastic (shear-thinning) behaviour, as seen by the decreasing viscosities with shear rate in Figure 15, which is desirable for tape casting (BITTERLICH; LUTZ; ROOSEN, 2002), because easy flow is required under the casting blade but should be slower after the tape is cast so it retains its planar shape with constant thickness. The rheological curve for the $\phi = 30$ vol.% sample did not present significant hysteresis, which is conversely noticeable for $\phi = 45$ vol.%. Non-thixotropic behaviour is usually appealing for the tape casting process (BITTERLICH; LUTZ; ROOSEN, 2002), because a variable apparent viscosity could cause non-uniform thickness in the tape. In log-log scale, near parallel lines are observed for shear stress versus strain rate curves at different solids loadings (Figure 14). They are however not exactly parallel because of the different n values presented in Table 3. In this table, it is possible to observe a pronounced effect of solids loading on the flow consistency index (k) and a less significant effect on the flow behaviour index (n).

Figure 14 – Comparison of rheological curves for 45 vol.%, 35 vol.% and 30 vol.% solids loading suspensions (Slurries D, E and F respectively) in log-log scale
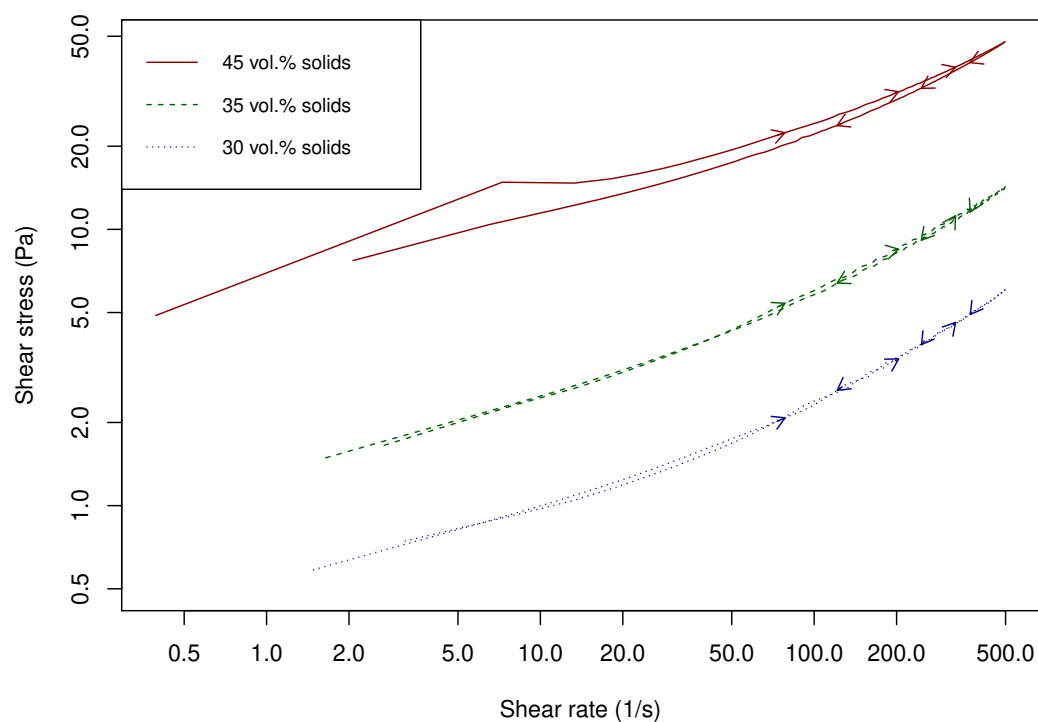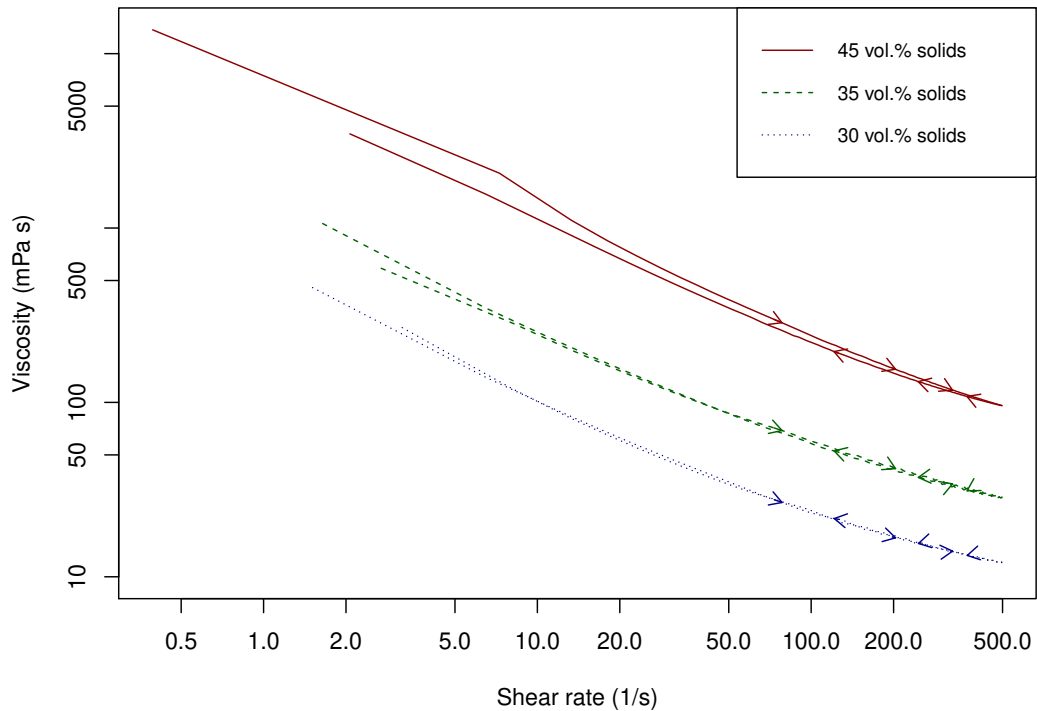
Figure 15 – Comparison of dynamic viscosity versus strain rate for different solids loadings in log-log scale

Table 3 – Rheological data fitted to power-law model $\tau = k\dot{\gamma}^n$ (k values are in SI units)

Slurry	ϕ (vol.%)	k	n	R^2
D	45	5.387	0.33	0.9544
E	35	0.7266	0.47	0.9863
F	30	0.2643	0.49	0.9819

Green tapes were characterised by thermogravimetric analysis (TGA). The results are shown in Figure 16, alongside the differential thermogravimetric curve (DTG). The plots are given as mass percentage and mass percentage rate as a function of temperature and present mainly the burning off of organic additives (debinding) at high temperature, with the main peaks present in the interval 200–500 °C. The first minor peak (< 100 °C) may be attributed to residual solvent loss. The only additives in considerable amount to result in the next observable peaks are the binder and the plasticizer, considering the small contents of dispersant and defoamer. Since more than two peaks are present, we conclude that the molar mass distribution of one of these ingredients must be bimodal. A temperature of 500 °C was chosen for debinding of tapes in conventional sintering and 600 °C for tapes to be used in fast firing, because elimination of residual organics in the first case is possible during the second heating ramp (see Figure 6 in section 3.1), whereas ideally total elimination of additives should be performed prior to fast firing.

Figure 16 – Thermogravimetric analysis and differential thermogravimetric analysis curves (tape from slurry A)
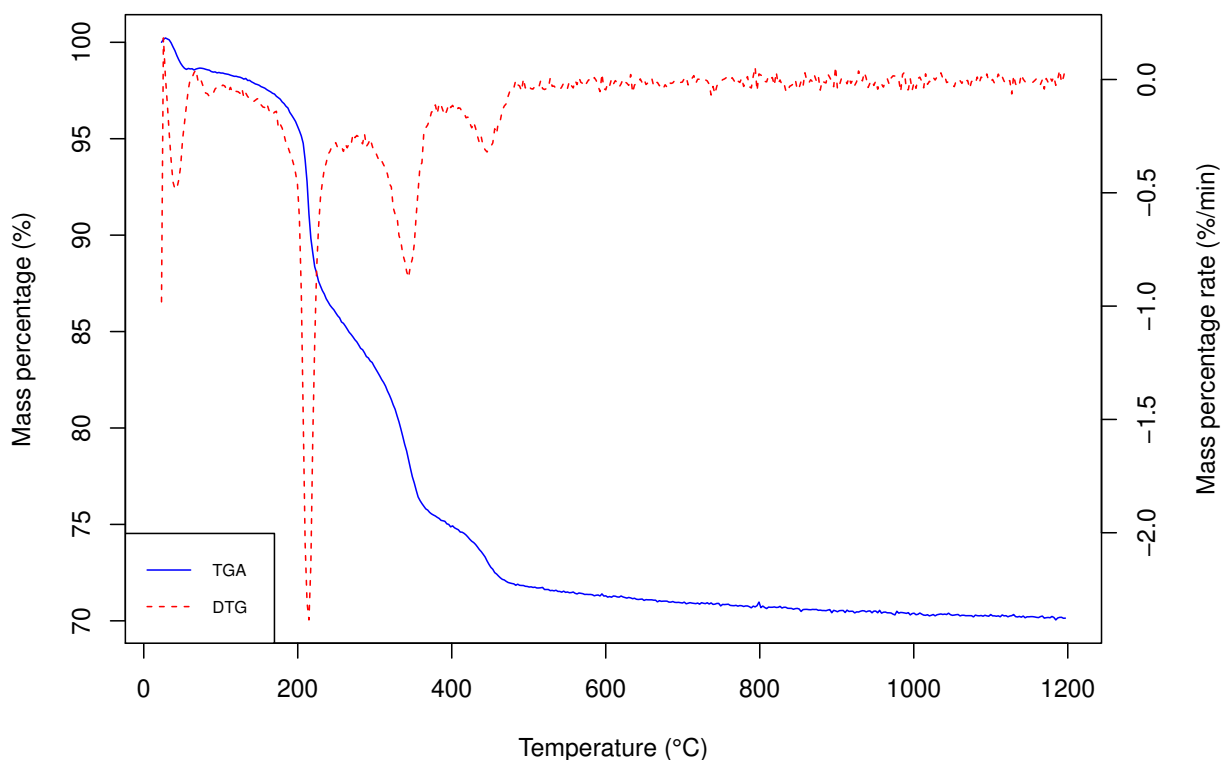
Some green tapes prepared in this work could not be further processed because of severe crack formation during the drying operation. One example is shown in Figure 17a. The difference between this tape (from slurry C) and the tape from slurry A (see Table 1 for compositions), which did not present any cracks, is mainly the presence of a plasticizer (polyethylene glycol, 22.5 wt.%) in slurry A, the total solids loading (30 vol.% for slurry A and 40 vol.% for slurry C) and the binder content (25 wt.% for slurry A and 35 wt.% for slurry C). In preliminary tests, a binder content of 25 wt.% was used, which did bring up crack formation. A hypothesis that a higher binder content (35 wt.%) would resolve the crack issue was proposed and disproved in the tests with slurry C. Thus a plasticizer was introduced, which completely inhibited crack formation and allowed the reduction in binder content in order not to overload the process with organics, which could induce the system to reduce to incohesive powder after debinding. In contrast, the overuse of plasticizer in some preliminary tests made the tape stretch upon removal from the substrate, which is also undesirable. The reduction in the solids loading was done to optimize the rheological behaviour, as described earlier in this section.

Figure 17 – (a) Crack pattern developed in tape from slurry C without plasticizer; (b) Green tape from slurry A in comparison, with no cracks
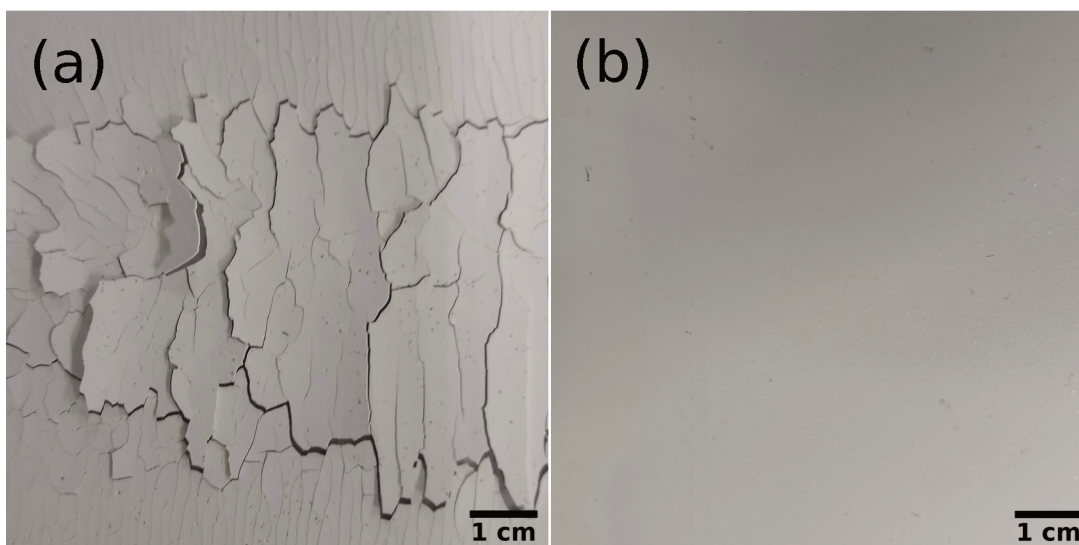
4.3   SINTERED TAPES

Sintered tapes were characterised in terms of porosity and bulk density by Archimedes method, real density by helium pycnometry, composition by X-ray diffraction (XRD), microstructure including grain size by scanning electron microscopy (SEM) and relative permittivity by frequency-dependent dielectric measurement.

The XRD patterns for the synthesized $TiNb_2O_7$ (all from slurry A) are shown in Figure 18. They conform to JCPDS no. 00-039-1407, which corresponds to a single monoclinic $TiNb_2O_7$ phase. This is valid for conventionally sintered tapes (CS) and fast-fired tapes at holding times of 2, 5 and 10 min (FF2, FF5 and FF10 respectively). This proves that a $TiNb_2O_7$ phase can be formed at very short times at high temperature. In fact, the time required to form a crystalline titanium niobate phase using a solid state reaction in this work is unprecedented, which is highlighted by Figure 2 (in section 2.1), and a crystallisation step was not necessary. This result concludes that fast firing is an adequate technique to produce thin flat $TiNb_2O_7$ tapes from titania and niobia precursors for various applications.

Figure 18 – XRD patterns of fast-fired and conventionally sintered tapes in comparison
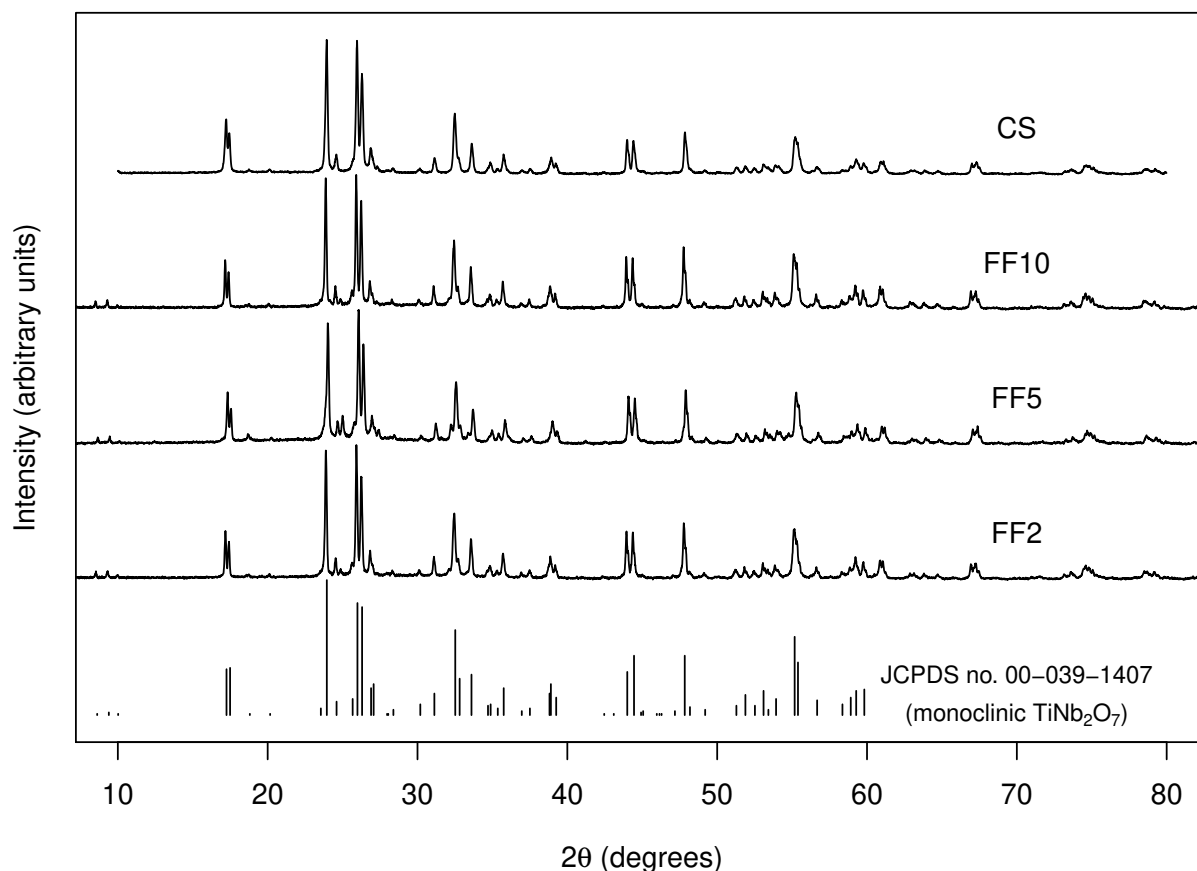
Open and total porosity and bulk density of tapes prepared from slurry A were determined using the Archimedes method. These results are presented in Table 4. In order to compute them, it was necessary to measure powder real density, $\rho_{TiNb_2O_7} = 4.39\,g\,cm^{-3}$ (measured for conventionally sintered tape from slurry A), by helium pycnometry.

Open porosity was close in magnitude to the total porosity for all tapes, which indicates that the porous space is interconnected. For FF2, the measured total porosity was 1% less than the open porosity, which is incoherent and thus attributed to uncertainty of the measurement.

Open porosities suggest that fabricated tapes could be used as membranes. The hydrophilicity of the tapes also corroborates with this (contact angle of 50°). The open porosity of FF5 was 34%, which can be compared to membranes for microfiltration of oily water with a porosity of 35%, studied by Mueller, Cen, and Davis (1997). The main drawback is nonetheless the fragility of more porous tapes. Mechanical strength and permeability should be measured if these tapes were to be applied as membranes. Nevertheless, the thin tapes could in prospect be applied on a thicker support, as in the case of most commercial membranes.

Table 4 – Porosity and bulk density of sintered tapes as measured by Archimedes method

	ε_{open} (%)	ε_{total} (%)	ρ_{bulk} (g cm^{-3})
FF2	50	49	2.2
FF5	34	35	2.8
FF10	29	29	3.1
CS	12	13	3.8

SEM images of the as-produced sintered tapes from slurry A are shown in Figure 19. The image of the conventionally sintered tape shows an abnormal phenomenon for microstructural development. It demonstrates a near regular elongated prismatic shape of the grains ("microrods"). This is not a common trait of sintered ceramics without any special treatment or structure-orienting additives. It could be attributed however to the crystal habit of the monoclinic $TiNb_2O_7$ phase.

Figure 19 – SEM images of the sintered tapes
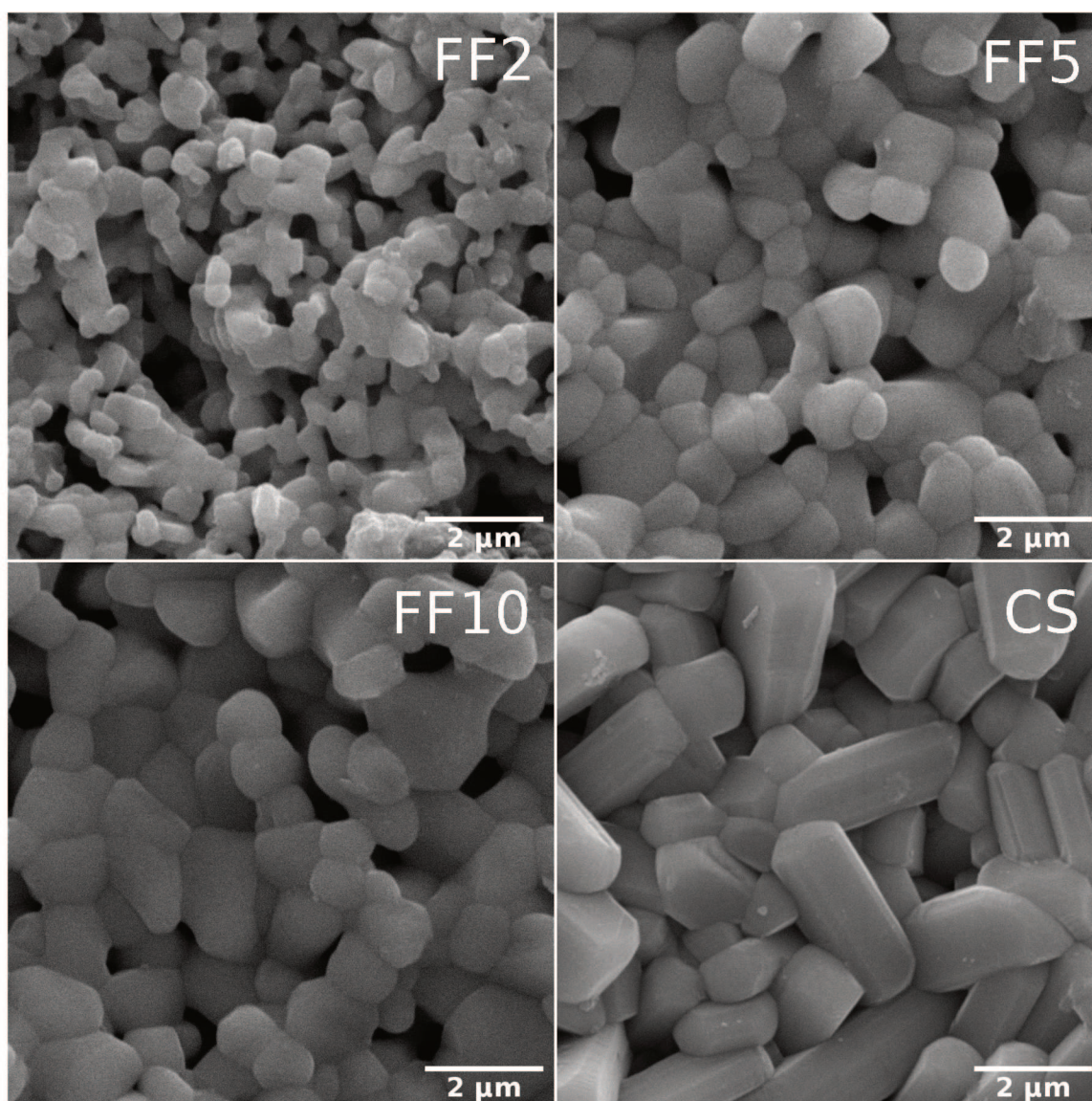
The plots of average grain size and bulk density for fast-fired and conventionally sintered tapes are shown in Figure 20. In Figure 20a, one sees the evolution trend of grain growth for fast-fired tapes. A significant growth (78 %) is observed in the interval of 2 to 5 min. Between 5 and 10 min, grain growth kinetics is slower and a 112 % growth percentage with respect to FF2 is observed for FF10. The conventionally sintered tapes had considerably coarser grains, with a 243 % growth with respect to FF2. The evolution of bulk density with the holding time (Figure 20b), related to the phenomenon of densification, also presented a more significant increase between 2–5 min than 5–10 min.

Figure 20 – (a) Average grain size as measured from SEM images and (b) Bulk density by Archimedes method
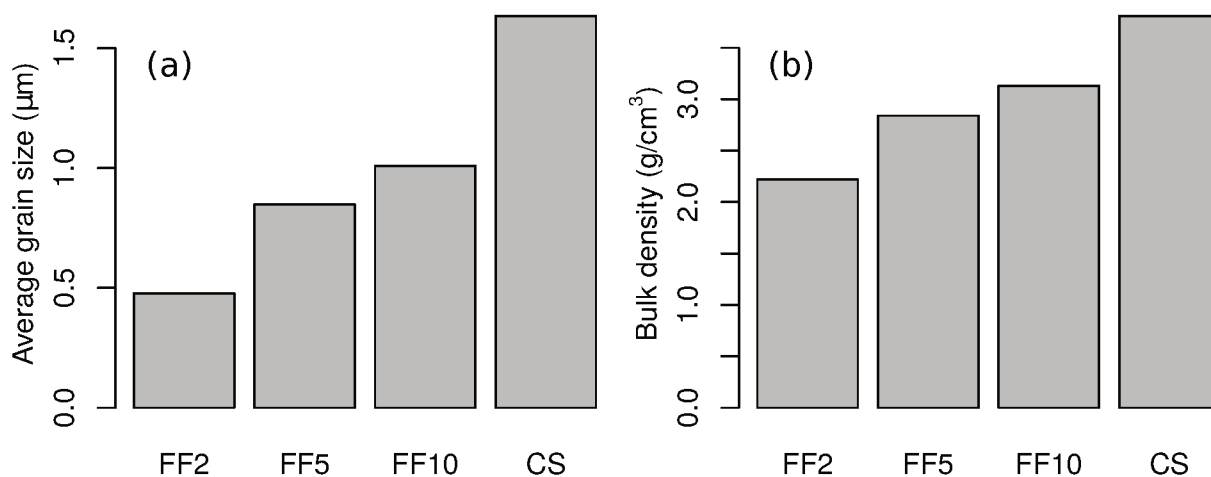
The dielectric constant as a function of frequency was measured for the conventionally sintered tape and the fast-fired (10 min) tape (both from slurry A). The plot is shown in Figure 21. The relative permittivity of a fast-fired tape (10 min) was close in magnitude to the relative permittivity measured for the conventionally sintered tape throughout the frequency range (20 Hz–2 MHz). The fading of the dielectric constant with frequency is known as dielectric dispersion, which is due to the failing of polarization mechanims at higher frequencies. The zero-frequency relative permittivity was ~ 10, which is similar to the value for graphite.

Figure 21 – Relative permittivity versus frequency for fast-fired (10 min) and conventionally sintered tapes
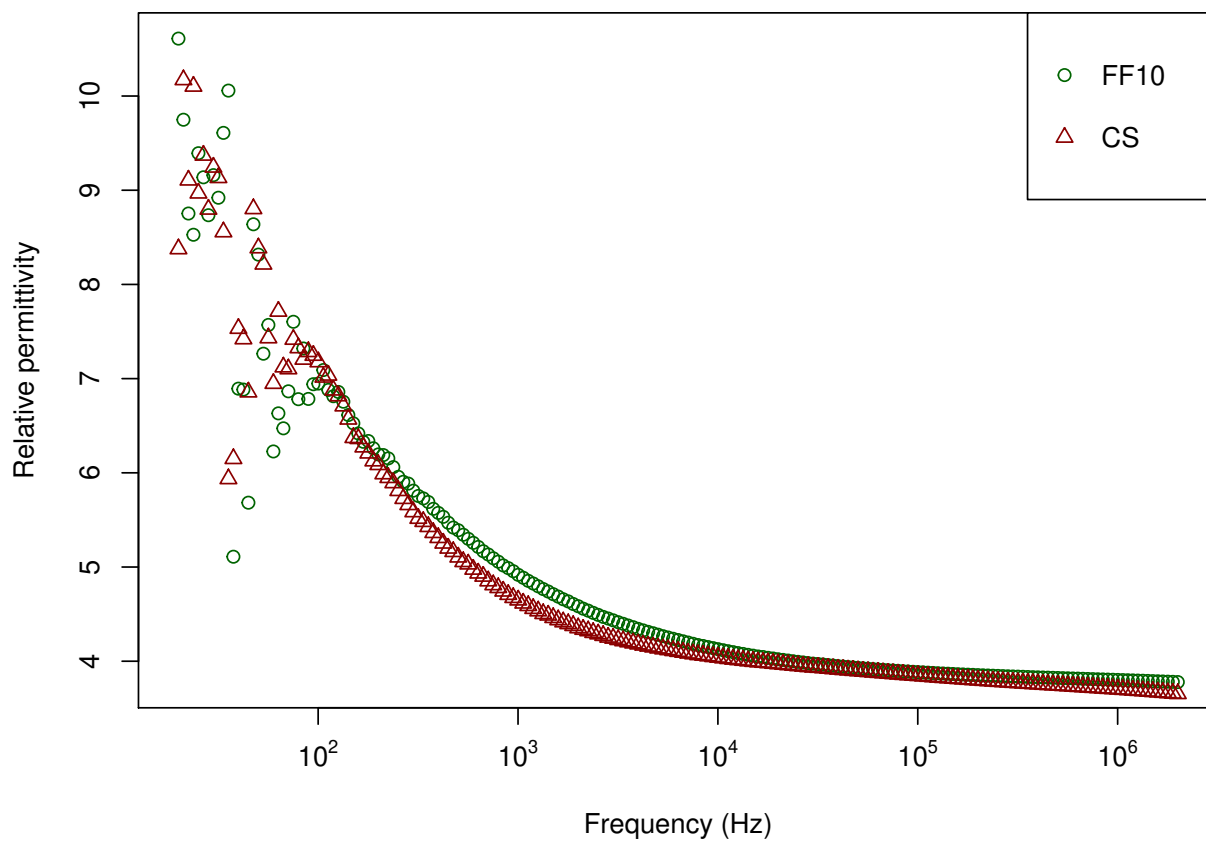
5 CONCLUDING REMARKS

This work was successful in attempting to simultaneously synthesize and sinter $TiNb_2O_7$ in a solid state reaction via fast firing. That is confirmed by XRD analysis of the sintered parts, which consist of pure crystalline $TiNb_2O_7$ for samples prepared with holding times of 2, 5 and 10 min. Furthermore, the material was also sintered conventionally, which produced a differentiated grain shape: near uniformly-sized elongated prisms ("microrods"). It also seems to be the first time fast firing has been applied as a sintering method for bodies shaped by tape casting (tapes), with a positive result indicating that the process could be potentially scaled-up for the manufacturing of thin tapes in an industrial setting.

Following the rheological study, we chose an optimal solids loading of 30 vol.%, given that higher amounts produced hysteresis, which is undesirable for tape casting. Pseudoplastic behaviour was observed for all tested suspensions, which is appealing for tape casting.

Crack formation during the drying operation was a major issue, since the occurrence of widespread cracks throughout a sample prohibited its continuation in the process (i.e. debinding and sintering). A significant improvement in this respect was achieved by introducing a plasticizer (polyethylene glycol) at a high content.

It was shown that it is possible to tailor the total and open porosities by changing the holding time in the furnace. The fast-fired tapes were highly porous while conventionally sintered tapes were in comparison much denser. It may also be noted that the tapes were hydrophilic. This is an indicative trait for the application of these tapes as filtration membranes. It is suggested for a future work to cast the thin tape on a macroporous structure to serve as a mechanical support for the functional membrane layer.

Although electrochemical measurements were not performed in this work, we propose rapid sintering/synthesis as a method to prepare porous $TiNb_2O_7$ tapes from the starting materials TiO_2 and Nb_2O_5 having in mind that titanium niobate is a well-established material in research for use as an anode material in lithium-ion batteries, and porous media with high surface area and small grain size are compelling for that application. It then follows that the next step in this line of research is to attempt the same process with nanoparticles as starting materials (titania and niobia), given nanostructured materials present superior electrochemical performance, and fast firing may be an appropriate method to mitigate unwanted grain coarsening. Since the solid state reaction and densification mechanism are diffusion-controlled, we hypothesize that the use of nanoparticles would not be an issue but in fact enhance the process kinetics with the only downside being that initial grain growth would be more rapid.

REFERENCES

ARAVINDAN, V.; SUNDARAMURTHY, J.; JAIN, A.; KUMAR, P. S.; LING, W. C.; RAMAKRISHNA, S.; SRINIVASAN, M. P.; MADHAVI, S. Unveiling $TiNb_2O_7$ as an insertion anode for lithium ion capacitors with high energy and power density. **ChemSusChem**, v. 7, n. 7, p. 1858–1863, 2014.

ASHISH, A.; ARUNKUMAR, P.; BABU, B.; MANIKANDAN, P.; SARANG, S.; SHAIJUMON, M. $TiNb_2O_7$/Graphene hybrid material as high performance anode for lithium-ion batteries. en. **Electrochimica Acta**, v. 176, p. 285–292, Sept. 2015. ISSN 00134686. DOI: `10.1016/j.electacta.2015.06.122`. Available from: `https://linkinghub.elsevier.com/retrieve/pii/S0013468615300505`. Visited on: 20 Dec. 2019.

BABICH, T. G.; ZAGORODNYUK, A. V.; TETERIN, G. A.; KHODOS, M. Y.; ZHIRNOVA, A. P. Nb_2O_5-TiO_2 system. **Zhurnal Neorganicheskoj Khimii**, v. 33, n. 4, p. 996–999, 1988.

BITTERLICH, B.; LUTZ, C.; ROOSEN, A. Rheological characterization of water-based slurries for the tape casting process. en. **Ceramics International**, v. 28, n. 6, p. 675–683, Jan. 2002. ISSN 02728842. DOI: `10.1016/S0272-8842(02)00027-5`. Available from: `https://linkinghub.elsevier.com/retrieve/pii/S0272884202000275`. Visited on: 31 Oct. 2019.

CHENG, Q.; LIANG, J.; LIN, N.; GUO, C.; ZHU, Y.; QIAN, Y. Porous $TiNb_2O_7$ nanospheres as ultra long-life and high-power anodes for lithium-ion batteries. en. **Electrochimica Acta**, v. 176, p. 456–462, Sept. 2015. ISSN 00134686. DOI: `10.1016/j.electacta.2015.07.038`. Available from: `https://linkinghub.elsevier.com/retrieve/pii/S0013468615301055`. Visited on: 20 Dec. 2019.

CHOI, S. H.; ALI, B.; CHOI, K. S.; HYUN, S. K.; SIM, J. J.; CHOI, W. J.; JOO, W.; LIM, J. H.; LEE, T. H.; KIM, T. S.; PARK, K. T. Reaction kinetics and morphological study of $TiNb_2O_7$ synthesized by solid-state reaction. **Archives of Metallurgy and Materials**, Vol. 62, iss. 2B, 2017. Available from: `http://yadda.icm.edu.pl/baztech/element/bwmeta1.element.baztech-3fc95f12-76d8-46cc-969e-79ef8358c278`. Visited on: 22 Nov. 2019.

DARAMALLA, V.; PENKI, T. R.; N., M.; S.B., K. Fabrication of $TiNb_2O_7$ thin film electrodes for Li-ion micro-batteries by pulsed laser deposition. en. **Materials Science and Engineering: B**, v. 213, p. 90–97, Nov. 2016. ISSN 09215107. DOI: `10.1016/j.mseb.2016.04.007`. Available from: `https://linkinghub.elsevier.com/retrieve/pii/S0921510716300265`. Visited on: 20 Dec. 2019.

DE HAART, L. G. J.; BOESSENKOOL, H. J.; BLASSE, G. Photoelectrochemical properties of titanium niobate ($TiNb_2O_7$) and titanium tantalate ($TiTa_2O_7$). en. **Materials Chemistry and Physics**, v. 13, n. 1, p. 85–90, July 1985. ISSN 0254-0584. DOI: `10.1016/0254-0584(85)90029-X`. Available from: `http://www.sciencedirect.com/science/article/pii/025405848590029X`. Visited on: 20 Dec. 2019.

EINSTEIN, A. Eine neue bestimmung der moleküldimensionen. **Annalen der Physik**, v. 324, n. 2, p. 289–306, 1906.

FALK, G. S.; BORLAF, M.; LÓPEZ-MUÑOZ, M. J.; NETO, J. R.; MORENO, R. Photocatalytic activity of nanocrystalline $TiNb_2O_7$ obtained by a colloidal sol-gel route. **Ceramics International**, v. 44, n. 6, p. 7122–7127, 2018.

FALK, G. S.; RODRIGUES NETO, J. B.; BORLAF, M.; GÓMEZ, S. Y.; NOVAES DE OLIVEIRA, A. P.; HOTZA, D. Fast microwave-assisted hydrothermal synthesis of $TiNb_2O_7$ nanoparticles. en. **International Journal of Ceramic Engineering & Science**, v. 1, n. 4, p. 235–240, Dec. 2019. ISSN 2578-3270, 2578-3270. DOI: `10.1002/ces2.10029`. Available from: `https://onlinelibrary.wiley.com/doi/abs/10.1002/ces2.10029`. Visited on: 22 Nov. 2019.

FEI, L.; XU, Y.; WU, X.; LI, Y.; XIE, P.; DENG, S.; SMIRNOV, S.; LUO, H. SBA-15 confined synthesis of $TiNb_2O_7$ nanoparticles for lithium-ion batteries. en. **Nanoscale**, v. 5, n. 22, p. 11102–11107, Oct. 2013. ISSN 2040-3372. DOI: `10.1039/C3NR03594H`. Available from: `https://pubs.rsc.org/en/content/articlelanding/2013/nr/c3nr03594h`. Visited on: 28 Nov. 2019.

GÓMEZ, S. Y.; SILVA, A. L. da; GOUVÊA, D.; CASTRO, R. H. R.; HOTZA, D. Nanocrystalline yttria-doped zirconia sintered by fast firing. en. **Materials Letters**, v. 166, p. 196–200, Mar. 2016. ISSN 0167-577X. DOI: `10.1016/j.matlet.2015.12.042`. Available from: `http://www.sciencedirect.com/science/article/pii/S0167577X15309952`. Visited on: 22 Nov. 2019.

GUO, B.; YU, X.; SUN, X.-G.; CHI, M.; QIAO, Z.-A.; LIU, J.; HU, Y.-S.; YANG, X.-Q.; GOODENOUGH, J. B.; DAI, S. A long-life lithium-ion battery with a highly porous $TiNb_2O_7$ anode for large-scale electrical energy storage. en. **Energy Environ. Sci.**, v. 7, n. 7, p. 2220–2226, 2014. ISSN 1754-5692, 1754-5706. DOI: `10.1039/C4EE00508B`. Available from: `http://xlink.rsc.org/?DOI=C4EE00508B`. Visited on: 22 Nov. 2019.

HAN, J.-T.; GOODENOUGH, J. B. 3-V full cell performance of anode framework $TiNb_2O_7$/spinel $LiNi_{0.5}Mn_{1.5}O_4$. **Chemistry of materials**, v. 23, n. 15, p. 3404–3407, 2011.

HAN, J.-T.; HUANG, Y.-H.; GOODENOUGH, J. B. New anode framework for rechargeable lithium batteries. en. **Chemistry of Materials**, v. 23, n. 8, p. 2027–2029, Apr. 2011. ISSN 0897-4756, 1520-5002. DOI: `10.1021/cm200441h`. Available from: `https://pubs.acs.org/doi/10.1021/cm200441h`. Visited on: 24 Dec. 2019.

HARMER, M. P.; BROOK, R. J. Fast firing- microstructural benefits. **Trans. J. Br. Ceram. Soc.**, v. 80, n. 5, p. 147, 1981.

HIEMENZ, P. C.; RAJAGOPALAN, R. **Principles of colloid and surface chemistry, third edition, revised and expanded**. [S.l.]: CRC Press, Mar. 1997. Google-Books-ID: CBvrS8rfPlYC. ISBN 978-0-8247-9397-5.

HOWATT, G. N.; BRECKENRIDGE, R. G.; BROWNLOW, J. M. Fabrication of thin ceramic sheets for capacitors*. en. **Journal of the American Ceramic Society**, v. 30, n. 8, p. 237–242, 1947. ISSN 1551-2916. DOI: `10.1111/j.1151-2916.1947.tb18889.x`. Available from: `https://ceramics.onlinelibrary.wiley.com/doi/abs/10.1111/j.1151-2916.1947.tb18889.x`. Visited on: 23 Sept. 2019.

HU, L.; LIN, C.; WANG, C.; YANG, C.; LI, J.; CHEN, Y.; LIN, S. $TiNb_2O_7$ nanorods as a novel anode material for secondary lithium-ion batteries. en. **Functional Materials Letters**, v. 09, n. 06, p. 1642004, Dec. 2016. ISSN 1793-6047, 1793-7213. DOI: `10.1142/S1793604716420042`. Available from: `https://www.worldscientific.com/doi/abs/10.1142/S1793604716420042`. Visited on: 24 Dec. 2019.

HU, Y.-S.; KIENLE, L.; GUO, Y.-G.; MAIER, J. High lithium electroactivity of nanometer-sized rutile TiO_2. **Advanced Materials**, v. 18, n. 11, p. 1421–1426, 2006. ISSN 1521-4095. DOI: `10.1002/adma.200502723`. Available from: `https://onlinelibrary.wiley.com/doi/abs/10.1002/adma.200502723`. Visited on: 27 Dec. 2019.

ISE, K.; MORIMOTO, S.; HARADA, Y.; TAKAMI, N. Large lithium storage in highly crystalline $TiNb_2O_7$ nanoparticles synthesized by a hydrothermal method as anodes for lithium-ion batteries. en. **Solid State Ionics**, v. 320, p. 7–15, July 2018. ISSN 01672738. DOI: `10.1016/j.ssi.2018.02.027`. Available from: `https://linkinghub.elsevier.com/retrieve/pii/S0167273817311633`. Visited on: 20 Dec. 2019.

JABBARI, M.; BULATOVA, R.; TOK, A. I. Y.; BAHL, C. R. H.; MITSOULIS, E.; HATTEL, J. H. Ceramic tape casting: A review of current methods and trends with emphasis on rheological behaviour and flow analysis. **Materials Science and Engineering: B**, v. 212, p. 39–61, Oct. 2016. ISSN 0921-5107. DOI: `10.1016/j.mseb.2016.07.011`. Available from: `http://www.sciencedirect.com/science/article/pii/S0921510716301088`. Visited on: 11 Sept. 2019.

JAT, R. A.; SAMUI, P.; GUPTA, N. K.; PARIDA, S. C. Synthesis, characterization and heat capacities of ternary oxides in the Ti–Nb–O system. en. **Thermochimica Acta**, v. 592, p. 31–36, Sept. 2014. ISSN 0040-6031. DOI: `10.1016/j.tca.2014.08.004`. Available from: `http://www.sciencedirect.com/science/article/pii/S0040603114003608`. Visited on: 21 Dec. 2019.

JAYARAMAN, S.; ARAVINDAN, V.; SURESH KUMAR, P.; CHUI LING, W.; RAMAKRISHNA, S.; MADHAVI, S. Exceptional performance of $TiNb_2O_7$ anode in all one-dimensional architecture by electrospinning. en. **ACS Applied Materials & Interfaces**, v. 6, n. 11, p. 8660–8666, June 2014. ISSN 1944-8244, 1944-8252. DOI: `10.1021/am501464d`. Available from: `https://pubs.acs.org/doi/10.1021/am501464d`. Visited on: 2 Jan. 2020.

JIAO, X.; HAO, Q.; XIA, X.; YAO, D.; OUYANG, Y.; LEI, W. Boosting long-cycle-life energy storage with holey graphene supported $TiNb_2O_7$ network nanostructure for lithium ion hybrid supercapacitors. en. **Journal of Power Sources**, v. 403, p. 66–75, Nov. 2018. ISSN 03787753. DOI: `10.1016/j.jpowsour.2018.09.050`. Available from: `https://linkinghub.elsevier.com/retrieve/pii/S0378775318310218`. Visited on: 20 Dec. 2019.

JO, C.; KIM, Y.; HWANG, J.; SHIM, J.; CHUN, J.; LEE, J. Block copolymer directed ordered mesostructured $TiNb_2O_7$ multimetallic oxide constructed of nanocrystals as high power li-ion battery anodes. en. **Chemistry of Materials**, v. 26, n. 11, p. 3508–3514, June 2014. ISSN 0897-4756, 1520-5002. DOI: `10.1021/cm501011d`. Available from: `https://pubs.acs.org/doi/10.1021/cm501011d`. Visited on: 22 Nov. 2019.

KANG, K.; MENG, Y. S.; BRÉGER, J.; GREY, C. P.; CEDER, G. Electrodes with high power and high capacity for rechargeable lithium batteries. en. **Science**, v. 311, n. 5763, p. 977–980, Feb. 2006. ISSN 0036-8075, 1095-9203. DOI: `10.1126/science.1122152`. Available from: `https://science.sciencemag.org/content/311/5763/977`. Visited on: 28 Nov. 2019.

KANG, S.-J. L. **Sintering: densification, grain growth, and microstructure**. Amsterdam: Elsevier, 2005. (Materials science & engineering). OCLC: 249434455. ISBN 978-0-7506-6385-4.

LARSON, R. G. Particulate suspensions. In: THE structure and rheology of complex fluids. New York: Oxford University Press, 1999. (Topics in chemical engineering). ISBN 978-0-19-512197-1.

LI, H.; ZHANG, Y.; TANG, Y.; ZHAO, F.; ZHAO, B.; HU, Y.; MURAT, H.; GAO, S.; LIU, L. $TiNb_2O_7$ nanowires with high electrochemical performances as anodes for lithium ion batteries. en. **Applied Surface Science**, v. 475, p. 942–946, May 2019. ISSN 01694332. DOI: `10.1016/j.apsusc.2019.01.045`. Available from:

`https://linkinghub.elsevier.com/retrieve/pii/S0169433219300558`. Visited on: 20 Dec. 2019.

LIU, G.; LIU, X.; ZHAO, Y.; JI, X.; GUO, J. Synthesis of Ag-coated $TiNb_2O_7$ composites with excellent electrochemical properties for lithium-ion battery. en. **Materials Letters**, v. 197, p. 38–40, June 2017. ISSN 0167577X. DOI: `10.1016/j.matlet.2017.03.145`. Available from: `https://linkinghub.elsevier.com/retrieve/pii/S0167577X17304937`. Visited on: 20 Dec. 2019.

LIU, G.; ZHAO, L.; SUN, R.; CHEN, W.; HU, M.; LIU, M.; DUAN, X.; ZHANG, T. Mesoporous $TiNb_2O_7$ microspheres as high performance anode materials for lithium-ion batteries with high-rate capability and long cycle-life. en. **Electrochimica Acta**, v. 259, p. 20–27, Jan. 2018. ISSN 00134686. DOI: `10.1016/j.electacta.2017.10.138`. Available from: `https://linkinghub.elsevier.com/retrieve/pii/S0013468617322600`. Visited on: 20 Dec. 2019.

LOU, S.; CHENG, X.; ZHAO, Y.; LUSHINGTON, A.; GAO, J.; LI, Q.; ZUO, P.; WANG, B.; GAO, Y.; MA, Y.; DU, C.; YIN, G.; SUN, X. Superior performance of ordered macroporous $TiNb_2O_7$ anodes for lithium ion batteries: Understanding from the structural and pseudocapacitive insights on achieving high rate capability. en. **Nano Energy**, v. 34, p. 15–25, Apr. 2017. ISSN 22112855. DOI: `10.1016/j.nanoen.2017.01.058`. Available from: `https://linkinghub.elsevier.com/retrieve/pii/S2211285517300654`. Visited on: 20 Dec. 2019.

LOU, S.; MA, Y.; CHENG, X.; GAO, J.; GAO, Y.; ZUO, P.; DU, C.; YIN, G. Facile synthesis of nanostructured $TiNb_2O_7$ anode materials with superior performance for high-rate lithium ion batteries. en. **Chemical Communications**, v. 51, n. 97, p. 17293–17296, 2015. ISSN 1359-7345, 1364-548X. DOI: `10.1039/C5CC07052J`. Available from: `http://xlink.rsc.org/?DOI=C5CC07052J`. Visited on: 15 July 2019.

LU, X.; JIAN, Z.; FANG, Z.; GU, L.; HU, Y.-S.; CHEN, W.; WANG, Z.; CHEN, L. Atomic-scale investigation on lithium storage mechanism in TiNb2O7, en. **Energy & Environmental Science**, v. 4, n. 8, p. 2638, 2011. ISSN 1754-5692, 1754-5706. DOI: `10.1039/c0ee00808g`. Available from: `http://xlink.rsc.org/?DOI=c0ee00808g`. Visited on: 21 Dec. 2019.

LUO, J.; PENG, J.; ZENG, P.; WU, Z.; LI, J.; LI, W.; HUANG, Y.; CHANG, B.; WANG, X. $TiNb_2O_7$ nano-particle decorated carbon cloth as flexible self-support anode material in lithium-ion batteries. en. **Electrochimica Acta**, v. 332, p. 135469, Feb. 2020. ISSN 00134686. DOI: `10.1016/j.electacta.2019.135469`. Available from: `https://linkinghub.elsevier.com/retrieve/pii/S0013468619323412`. Visited on: 20 Dec. 2019.

MISTLER, R. E.; TWINAME, E. R. Tape casting: theory and practice, 2000.

MORENO, V.; AGUILAR, J. L.; HOTZA, D. 8YSZ tapes produced by aqueous tape casting. In: MATERIALS Science Forum. [S.l.]: Trans Tech Publ, 2012. p. 752–757.

MUELLER, J.; CEN, Y.; DAVIS, R. H. Crossflow microfiltration of oily water. en. **Journal of Membrane Science**, v. 129, n. 2, p. 221–235, July 1997. ISSN 0376-7388. DOI: `10.1016/S0376-7388(96)00344-4`. Available from: `http://www.sciencedirect.com/science/article/pii/S0376738896003444`. Visited on: 2 Dec. 2019.

MUELLER, S.; LLEWELLIN, E. W.; MADER, H. M. The rheology of suspensions of solid particles. en. **Proceedings of the Royal Society A: Mathematical, Physical and Engineering Sciences**, v. 466, n. 2116, p. 1201–1228, Apr. 2010. ISSN 1364-5021, 1471-2946. DOI: `10.1098/rspa.2009.0445`. Available from: `http://rspa.royalsocietypublishing.org/cgi/doi/10.1098/rspa.2009.0445`. Visited on: 27 Nov. 2018.

NOH, H.; CHOI, W. Preparation of a $TiNb_2O_7$ microsphere using formic acid and wrapping with reduced graphene oxide for anodes in lithium ion batteries. en. **Journal of The Electrochemical Society**, v. 163, n. 6, a1042–a1049, 2016. ISSN 0013-4651, 1945-7111. DOI: `10.1149/2.1181606jes`. Available from: `http://jes.ecsdl.org/lookup/doi/10.1149/2.1181606jes`. Visited on: 20 Dec. 2019.

PARK, H.; SONG, T.; PAIK, U. Porous $TiNb_2O_7$ nanofibers decorated with conductive $Ti_{1x}Nb_xN$ bumps as a high power anode material for Li-ion batteries. en. **Journal of Materials Chemistry A**, v. 3, n. 16, p. 8590–8596, 2015. ISSN 2050-7488, 2050-7496. DOI: `10.1039/C5TA00467E`. Available from: `http://xlink.rsc.org/?DOI=C5TA00467E`. Visited on: 21 Dec. 2019.

PARK, H.; WU, H. B.; SONG, T.; DAVID LOU, X. W.; PAIK, U. Porosity-controlled $TiNb_2O_7$ microspheres with partial nitridation as a practical negative electrode for high-power lithium-ion batteries. en. **Advanced Energy Materials**, v. 5, n. 8, p. 1401945, Apr. 2015. ISSN 16146832. DOI: `10.1002/aenm.201401945`. Available from: `http://doi.wiley.com/10.1002/aenm.201401945`. Visited on: 23 Nov. 2019.

PHAM-CONG, D.; CHOI, J. H.; YUN, J.; BANDARENKA, A. S.; KIM, J.; BRAUN, P. V.; JEONG, S. Y.; CHO, C. R. Synergistically enhanced electrochemical performance of hierarchical $MoS_2/TiNb_2O_7$ hetero-nanostructures as anode materials for li-ion batteries. en. **ACS Nano**, v. 11, n. 1, p. 1026–1033, Jan. 2017. ISSN 1936-0851, 1936-086X. DOI: `10.1021/acsnano.6b07666`. Available from: `https://pubs.acs.org/doi/10.1021/acsnano.6b07666`. Visited on: 24 Dec. 2019.

POSSAMAI, T. S.; OBA, R.; NICOLAU, V. P.; HOTZA, D.; GARCÍA, D. E. Numerical simulation of the fast firing of alumina in a box furnace. en. **Journal of the American Ceramic Society**, v. 95, n. 12, p. 3750–3757, 2012. ISSN 1551-2916. DOI: `10.1111/j.1551-2916.2012.05432.x`. Available from:

`https://ceramics.onlinelibrary.wiley.com/doi/abs/10.1111/j.1551-2916.2012.05432.x`. Visited on: 17 Jan. 2020.

REICH, C. M.; KAISER, A.; IRVINE, J. T. S. Niobia based rutile materials as SOFC anodes. en. **FUEL CELLS**, n. 3, p. 7, 2001.

ROTH, R.; COUGHANOUR, L. Phase equilibrium relations in the systems titania-niobia and zirconia-niobia. en. **Journal of Research of the National Bureau of Standards**, v. 55, n. 4, p. 209, Oct. 1955. ISSN 0091-0635. DOI: `10.6028/jres.055.023`. Available from: `https://nvlpubs.nist.gov/nistpubs/jres/55/jresv55n4p209_A1b.pdf`. Visited on: 25 Dec. 2019.

TAKAMI, N.; ISE, K.; HARADA, Y.; IWASAKI, T.; KISHI, T.; HOSHINA, K. High-energy, fast-charging, long-life lithium-ion batteries using $TiNb_2O_7$ anodes for automotive applications. en. **Journal of Power Sources**, v. 396, p. 429–436, Aug. 2018. ISSN 03787753. DOI: `10.1016/j.jpowsour.2018.06.059`. Available from: `https://linkinghub.elsevier.com/retrieve/pii/S0378775318306554`. Visited on: 20 Dec. 2019.

TANG, K.; MU, X.; AKEN, P. A. van; YU, Y.; MAIER, J. "Nano-pearl-string" $TiNb_2O_7$ as anodes for rechargeable lithium batteries. en. **Advanced Energy Materials**, v. 3, n. 1, p. 49–53, Jan. 2013. ISSN 16146832. DOI: `10.1002/aenm.201200396`. Available from: `http://doi.wiley.com/10.1002/aenm.201200396`. Visited on: 22 Nov. 2019.

WANG, X.; SHEN, G. Intercalation pseudo-capacitive $TiNb_2O_7$@ carbon electrode for high-performance lithium ion hybrid electrochemical supercapacitors with ultrahigh energy density. **Nano Energy**, v. 15, p. 104–115, 2015.

WEN, X.; MA, C.; DU, C.; LIU, J.; ZHANG, X.; QU, D.; TANG, Z. Enhanced electrochemical properties of vanadium-doped titanium niobate as a new anode material for lithium-ion batteries. en. **Electrochimica Acta**, v. 186, p. 58–63, Dec. 2015. ISSN 0013-4686. DOI: `10.1016/j.electacta.2015.10.158`. Available from: `http://www.sciencedirect.com/science/article/pii/S0013468615307398`. Visited on: 21 Dec. 2019.

YOON, S.; LEE, S.-Y.; NGUYEN, T. L.; KIM, I. T.; WOO, S.-G.; CHO, K. Y. Controlled synthesis of dual-phase carbon-coated Nb_2O_5/$TiNb_2O_7$ porous spheres and their Li-ion storage properties. en. **Journal of Alloys and Compounds**, v. 731, p. 437–443, Jan. 2018. ISSN 09258388. DOI: `10.1016/j.jallcom.2017.10.051`. Available from: `https://linkinghub.elsevier.com/retrieve/pii/S0925838817334655`. Visited on: 20 Dec. 2019.

YU, H.; LAN, H.; YAN, L.; QIAN, S.; CHENG, X.; ZHU, H.; LONG, N.; SHUI, M.; SHU, J. $TiNb_2O_7$ hollow nanofiber anode with superior electrochemical performance in rechargeable lithium ion batteries. en. **Nano Energy**, v. 38, p. 109–117, Aug. 2017. ISSN 22112855. DOI: `10.1016/j.nanoen.2017.05.057`. Available from:

`https://linkinghub.elsevier.com/retrieve/pii/S2211285517303452`. Visited on: 20 Dec. 2019.

YU, Z.; WACLAWIK, E. R.; WANG, Z.; GU, X.; YUAN, Y.; ZHENG, Z. Dual modification of $TiNb_2O_7$ with nitrogen dopants and oxygen vacancies for selective aerobic oxidation of benzylamine to imine under green light. en. **Journal of Materials Chemistry A**, v. 5, n. 9, p. 4607–4615, 2017. ISSN 2050-7488, 2050-7496. DOI: `10.1039/C6TA11061D`. Available from: `http://xlink.rsc.org/?DOI=C6TA11061D`. Visited on: 21 Dec. 2019.